EUROPEAN RESPIRATORY *journal*

FLAGSHIP SCIENTIFIC JOURNAL OF ERS

Early View

Original research article

GPR183 antagonism reduces macrophage infiltration in influenza and SARS-CoV-2 infection

Cheng Xiang Foo, Stacey Bartlett, Keng Yih Chew, Minh Dao Ngo, Helle Bielefeldt-Ohmann, Buddhika Jayakody Arachchige, Benjamin Matthews, Sarah Reed, Ran Wang, Christian Smith, Matthew J. Sweet, Lucy Burr, Kavita Bisht, Svetlana Shatunova, Jane E. Sinclair, Rhys Parry, Yuanhao Yang, Jean-Pierre Lévesque, Alexander Khromykh, Mette Marie Rosenkilde, Kirsty R. Short, Katharina Ronacher

Please cite this article as: Foo CX, Bartlett S, Chew KY, *et al*. GPR183 antagonism reduces macrophage infiltration in influenza and SARS-CoV-2 infection. *Eur Respir J* 2022; in press (https://doi.org/10.1183/13993003.01306-2022).

GPR183 antagonism reduces macrophage infiltration in influenza and SARS-CoV-2 infection

Cheng Xiang Foo[1#], Stacey Bartlett[1#], Keng Yih Chew[2,] Minh Dao Ngo[1], Helle Bielefeldt-Ohmann[2,3], Buddhika Jayakody Arachchige[4], Benjamin Matthews[4], Sarah Reed[4], Ran Wang[1], Christian Smith[1], Matthew J. Sweet[3,5], Lucy Burr[6], Kavita Bisht[1], Svetlana Shatunova[1], Jane E. Sinclair[2], Rhys Parry[2], Yuanhao Yang[1], Jean-Pierre Lévesque[1], Alexander Khromykh[2,3], Mette Marie Rosenkilde[7], Kirsty R. Short[2,3] and Katharina Ronacher[1,3*]

[1]Mater Research Institute, Translational Research Institute, The University of Queensland, Brisbane, Australia

[2]School of Chemistry and Molecular Biosciences, The University of Queensland, Brisbane, Australia

[3]Australian Infectious Diseases Research Centre, The University of Queensland, Brisbane, Australia

[4]Centre for Clinical Research, The University of Queensland, Brisbane, Australia

[5]Institute for Molecular Bioscience (IMB), IMB Centre for Inflammation and Disease Research, The University of Queensland, Brisbane, Australia

[6]Department of Respiratory Medicine, Mater Adult Hospital, South Brisbane, Queensland, Australia

[7]Department of Biomedical Sciences, University of Copenhagen, Copenhagen, Denmark

[#] Contributed equally to this work.

*Correspondence:

Katharina Ronacher: Mater Research Institute-The University of Queensland, Translational Research Institute, 37 Kent Street, Brisbane 4102, QLD, Australia; email: Katharina.Ronacher@mater.uq.edu.au; phone: +61 7 3443 7633

Author Summary: Viral infections trigger oxysterol production in the lung, attracting macrophages via GPR183. Antagonising GPR183 reduced inflammation and disease severity in SARS-CoV-2 infection, making GPR183 a putative target for therapeutic intervention.

Abstract

Rationale: Severe viral respiratory infections are often characterised by extensive myeloid cell infiltration and activation and persistent lung tissue injury. However, the immunological mechanisms driving excessive inflammation in the lung remain poorly understood.

Objectives: To identify the mechanisms that drive immune cell recruitment in the lung during viral respiratory infections and identify novel drug targets to reduce inflammation and disease severity.

Methods: Preclinical murine models of influenza virus and severe acute respiratory coronavirus 2 (SARS-CoV-2) infection.

Results: Oxidised cholesterols and the oxysterol-sensing receptor GPR183 were identified as drivers of monocyte-macrophage infiltration to the lung during influenza virus (IAV) and SARS-CoV-2 infection. Both IAV and SARS-CoV-2 infection upregulated the enzymes cholesterol 25-hydroxylase (CH25H) and cytochrome P450 family 7 subfamily member B1 (CYP7B1) in the lung, resulting in local production of the oxidised cholesterols 25-hydroxycholesterol (25-OHC) and 7α,25-dihydroxycholesterol (7α,25-OHC). Loss-of-function mutation of GPR183, or treatment with a GPR183 antagonist, reduced macrophage infiltration and inflammatory cytokine production in the lungs of IAV- or SARS-CoV-2-infected mice. The GPR183 antagonist significantly attenuated the severity of SARS-CoV-2 infection and viral loads. Analysis of single cell RNASeq data on bronchoalveolar lavage samples from healthy controls and COVID-19 patients with moderate and severe disease revealed that *CH25H, CYP7B1* and *GPR183* are significantly upregulated in macrophages during COVID-19.

Conclusion: This study demonstrates that oxysterols drive inflammation in the lung via GPR183 and provides the first preclinical evidence for therapeutic benefit of targeting GPR183 during severe viral respiratory infections.

Introduction

Severe viral respiratory infections including influenza and COVID-19 are associated with extensive myeloid cell recruitment to the lung, which can lead to severe tissue injury and the development of acute respiratory distress syndrome (ARDS) [1]. A shift in lung macrophage composition and function is associated with COVID-19 severity. A study of >600 hospitalised patients found that in severe cases resident alveolar macrophages were depleted and replaced by large numbers of inflammatory monocyte-derived macrophages [2]. Rapid monocyte-macrophage infiltration of the lung during the acute phase of severe acute respiratory coronavirus 2 (SARS-CoV-2) infection is replicated in animal models [3, 4].

Oxidised cholesterols have recently emerged as markers of inflammation in the lung. Oxysterols were increased in bronchoalveolar lavage fluid (BALF) from inflamed airways after allergen challenge and correlated with infiltrating leukocytes [5]. They were also increased in the sputum from patients with chronic obstructive pulmonary disease correlating with disease severity [6, 7] and in the lungs of mice after lipopolysaccharide (LPS)-induced lung inflammation [8]. However, the role of oxysterols in the lung during viral respiratory infections has not been investigated.

Oxysterols have a range of receptors sharing a common role in inflammation [9]. One oxysterol pathway leads to the production of 7α,25-hydroxycholesterol (7α,25-OHC), via cholesterol 25-hydroxylase (CH25H) and cytochrome P450 family 7 subfamily B member 1 (CYP7B1) [9, 10]. 7α,25-OHC can subsequently be metabolised by hydroxy-delta-5-steroid dehydrogenase, 3 beta- and steroid delta isomerase7 (HSD3B7) (**Figure 1A**). 7α,25-OHC is the endogenous high affinity agonist of the oxysterol-sensing G protein-coupled receptor GPR183 [11, 12]. GPR183 is expressed on cells of the innate and adaptive immune systems, including macrophages, dendritic cells, innate lymphoid cells, eosinophils and T and B lymphocytes [5, 13, 14]. With its oxysterol ligands GPR183 facilitates the chemotactic distribution of immune cells to secondary lymphoid organs [9, 11, 13, 15]. *In vitro* GPR183 mediates migration of human and mouse macrophages towards a 7α,25-OHC gradient [16, 17].

In this study, we hypothesised that viral respiratory infections lead to the production of oxysterols in the lung contributing to excessive immune cell infiltration and inflammation. We show that oxysterols drive GPR183-dependent monocyte-macrophage infiltration in preclinical models of IAV and SARS-CoV-2 infection and identify GPR183 is a host target for therapeutic intervention to mitigate disease severity in viral respiratory infections.

Methodology

Ethics and biosafety

All experiments were approved by the Animal Ethics Committee (MRI-UQ/596/18, AE000186) and the Institutional Biosafety Committee of the University of Queensland (IBC/465B/MRI/TRI/AIBN/2021).

Viral Strains

Virus stocks of A/H1N1/Auckland/1/2009(H1N1), referred to as influenza A virus (IAV), were prepared in embryonated chicken eggs. A mouse-adapted SARS-CoV-2 strain was obtained through serial passage of SARS-CoV-2 (B.1.351; hCoV-19/Australia/QLD1520/2020, GISAID accession EPI_ISL_968081, collected on 29 December 2020, kindly provided by Queensland Health Forensic and Scientific

Services). A description of the mouse-adaption and genomic sequencing data for the SARS-CoV-2 strain can be found in the supplemental methods (**Figure S1**). IAV viral titres were determined by plaque assays on Madin-Darby canine kidney (MDCK) and SARS-CoV-2 plaque assays on Vero E6 cells as described in the supplement.

Mouse models

Gpr183$^{\mathrm{tm1Lex}}$ were obtained from Lexicon Pharmaceuticals (The Woodlands, USA), back-crossed to a C57BL/6J background and bred in-house. Eight to 10-week-old C57BL/6J and *Gpr183*$^{\mathrm{tm1Lex}}$ (*Gpr183*$^{-/-}$) mice were anesthetized with 4% isoflurane and infected intranasally with 5,500 PFU of IAV A/Auckland/01/09 (H1N1). For SARS-CoV-2 infection, C57BL/6J and *Gpr183*$^{-/-}$ mice were anesthetized with ketamine/Xylazine (80mg/kg/5mg/kg) and infected intranasally with 8×10^4 PFU of mouse-adapted SARS-CoV-2. Lungs were collected at specified timepoints for subsequent downstream analysis as described in supplemental data. The GPR183 antagonist NIBR189 (7.6 mg/kg) in vehicle (0.5% carboxymethylcellulose/0.5% Tween-80) or vehicle only was administrated by oral gavage from 1 dpi, twice daily at 12-hour intervals until the end of the experiment.

RNA isolation and RT-qPCR

Total RNA was isolated using ISOLATE II RNA Mini Kit (Bioline Reagents Ltd., London, UK) as previously described [18, 19]. The list of primers is provided in **Table S1**. The relative expression (RE) of each gene normalised to the reference gene (Hypoxanthine-guanine phosphoribosyltransferase; *Hprt*) was determined using the $2^{-\Delta Ct}$ method.

Oxysterol extraction and mass spectrometric quantitation

The oxysterol extraction and quantification methods were adapted from Ngo et al. [18] as described in the supplemental information.

Cytokine quantification using ELISA

Cytokines in lung homogenates were measured with DuoSet ELISA (IFNβ (DY8234-05), IFNγ (DY485), IFNλ (DY1789B), IL-6 (DY406), TNFα (DY410), IL-1β (DY401), IL-10 (DY417) and CCL2 (DY479), R&D systems) according to the manufacturer's protocol.

Flow cytometry

Flow cytometry was performed on single cell suspensions from digested lungs and blood as described in detail in the supplement.

Immunohistochemistry

Immunohistochemistry (IHC) was performed on deparaffinized/rehydrated lung sections by immunolabelling with antibodies against SARS-CoV-2 nucleocapsid protein (40143-R040 Sino Biological), IBA1 (019-19741; NovaChem), CH25H (BS-6480R, Bioss Antibodies), CYP7B1 (BS-5052R, Bioss Antibodies) and isotype control (rabbit IgG 31235, Thermo Fisher Scientific) diluted in Da Vinci Green Diluent (PD900, Biocare Medical) followed by incubation with horseradish peroxidase (HRP)-conjugated goat anti-rabbit Ig antibody (1:200) (ab6721, Abcam). See supplementary data for details. Isotype controls are shown in (**Figure S2**).

Statistical analysis

Data were analysed on GraphPad Prism software. Data were assessed for normality using Shapiro-Wilk test. Spearman rank correlation was used to analyse correlations. For two group comparisons, parametric Student's two-tailed t test was used for normally distributed data while nonparametric Mann-Whitney U test was used for data that deviate from normality.

Results

IAV infection increases CH25H and CYP7B1 expression and oxysterol production in the lung

To investigate whether IAV infection induces the production of oxidised cholesterols, mice were infected with IAV (**Figure 1b**) and mRNA expression of oxysterol-producing enzymes was determined in lung tissue. *Ch25h* and *Cyp7b1* mRNA were increased in lungs of IAV-infected mice compared to uninfected animals, whereas *Hsd3b7* was downregulated in the lung 7 days post infection (dpi) (**Figure 1c,** upper panel). Similarly, CH25H and CYP7B1 proteins were also increased while HSD3B7 remained constant, as demonstrated by immunohistochemical labelling of lung sections with antibodies detecting CH25H, CYP7B1 and HSD3B7 (**Figure 1c,** lower panel). The induction of oxysterol-producing enzymes was associated with increased concentrations of the oxysterols 7α,25-OHC and 25-OHC in lung homogenates (**Figure 1d**, left panels) and bronchoalveolar lavage fluid (BALF) (**Figure 1d**, right panels) from IAV-infected animals at both 3 and 7 dpi. In uninfected lungs, 7α,25-OHC was undetectable in most samples tested. *Ch25h* and *Cyp7b1* mRNA were increased in the bronchoalveolar lavage (BAL) cell pellet of IAV-infected mice compared to uninfected animals while *Hsd3b7* remained unchanged **(Figure S3a).**

Consistent with the increase in oxysterols, *Gpr183* mRNA was increased at 3 and 7 dpi in both BAL cells (**Figure S3a**) and lung tissue (**Figure S3b**), suggesting increased expression and/or recruitment of GPR183-expressing immune cells to the lung upon infection. *Gpr183* expression was positively correlated with *Ch25h* and *Cyp7b1* (**Figure S3c**).

Gpr183$^{-/-}$ mice have reduced macrophage infiltration into the lungs upon IAV infection

To investigate whether oxysterol-mediated immune cell recruitment is dependent on the oxysterol-sensing GPR183, we performed experiments in mice genetically deficient in *Gpr183* (*Gpr183*$^{-/-}$). *Gpr183*$^{-/-}$ mice exhibit normal gross phenotype [20], had normal circulating monocyte numbers and comparable numbers of macrophage colony forming units (CFU-M) in the bone marrow to C57BL/6 mice (**Figure S4**) suggesting comparable monopoiesis in *Gpr183*$^{-/-}$ mice. However, upon infection with IAV, *Gpr183*$^{-/-}$ mice had lower IBA1^{+} macrophage numbers in the lung at 3 and 7 dpi compared to infected C57BL/6J controls (**Figure 2a**). *Gpr183* expression was positively correlated with mRNA expression of the pro-inflammatory cytokines *Il6, Tnf* and *Ccl2* in C57BL/6J mice (**Figure S5**) and reduced macrophage infiltration in *Gpr183*$^{-/-}$ mice was associated with reduced *Il6* and *Tnf,* but not *Ccl2* at 7 dpi (**Figure S6**). Body weights and viral titres through the course of IAV infection were comparable across the genotypes (**Figure S7**). These results demonstrate that lack of GPR183 reduces macrophage infiltration into the lung upon IAV infection which is associated with reduced pro-inflammatory cytokine expression.

GPR183 antagonism reduces macrophage infiltration

To investigate whether GPR183 is a putative therapeutic target to reduce inflammation, the GPR183 antagonist NIBR189 [11, 17] was administered to C57BL/6J mice twice daily starting from 24 h post-infection until the end of the experiment (**Figure 2b**). Like *Gpr183*$^{-/-}$ mice, C57BL/6J animals treated with

NIBR189 had significantly reduced macrophage infiltration into the lung both at 3 and 7 dpi as determined by IHC (**Figure 2c**).

In addition, flow cytometry analysis was performed on lung single cell suspensions from C57BL/6J and *Gpr183*$^{-/-}$ mice treated with NIBR189 and vehicle, respectively, using a previously published gating strategy [21] (**Figure S8**). NIBR189-treated C57BL/6J mice and *Gpr183*$^{-/-}$ mice had lower percentages of recruited/infiltrated macrophages (F480^{high}/CD11b^{+}/Ly6G^{-}/SigF^{-}) (**Figure 3a**) compared to vehicle-treated C57BL/6J animals after IAV infection. NIBR189 treatment did not change the percentages of other immune cell subsets in the lung, including neutrophils (B220^{-}/CD3^{-}/Ly6G^{+}/CD11b^{+}) (**Figure 3a**), CD4^{+} T cells, CD8^{+} T cells, B cells, DCs, and alveolar macrophages (**Figure S9, S10**). Body weights and lung viral loads were not affected by genotype or treatment (**Figure S11**).

These results demonstrate that NIBR189 significantly reduced macrophage infiltration to the lung without affecting the recruitment of other immune cell subsets.

GPR183 antagonism reduces IAV-induced pro-inflammatory cytokine concentrations

We next determined if the reduced macrophage infiltration mediated by NIBR189 results in reduced inflammatory cytokine production in the lung. At 3 dpi, no significant differences in cytokine production were observed between treatment groups (**Figure S12**). However, IAV-Infected C57BL/6J mice treated with NIBR189 had significantly lower concentrations of IL-6, TNF and IFNβ (**Figure 3b**) at 7 dpi. This was comparable to the phenotype of IAV-infected *Gpr183*$^{-/-}$ mice, with NIBR189 treatment having no additional effect in mice deficient in GPR183. In addition, no significant differences were observed in IFNλ across the two timepoints (**Figure 3b**

and Figure S12) demonstrating that the GPR183 antagonist treatment does not negatively impact the production of type III IFNs which are important for viral control in the lung [22]. No differences between treatment groups were observed at either timepoint for protein concentrations of IL-1β, CCL2 or IFNγ between treatment groups (**Figure S12 and S13**). Thus, GPR183 can be inhibited pharmacologically to reduce proinflammatory cytokines upon severe IAV infection.

GPR183 antagonism reduces SARS-CoV-2 infection severity

Excessive macrophage infiltration and activation is a hallmark of severe COVID-19 [2, 23]. To evaluate whether the benefits of inhibiting GPR183 extend to SARS-CoV-2 infection, we established a mouse-adapted SARS-CoV-2 strain by passaging the Beta variant of SARS-CoV-2 (B.1.351) four times in C57BL/6J mice. This resulted in a virus that contained a mutation in NSP5 and caused clinical signs (weight loss) in infected mice (**Figure S1**). Consistent with the IAV infection results, mRNA expression of *Ch25h* and *Cyp7b1* was significantly upregulated in the lungs of SARS-CoV-2 infected mice compared to uninfected mice while *Hsd3b7* remained unchanged (**Figure 4a**). This was confirmed also at the protein level by IHC (**Figure 4b,c**). Further, 25-OHC and 7α,25-OHC concentrations in lung homogenates (**Figure 4d,** left panels) and BALF (**Figure 4d,** right panels) were significantly increased at 2 dpi, returning to uninfected levels by 5 dpi by which time the animals began to recover from the infection. *Ch25h and Gpr183 was also increased* in BAL cells of SARS-CoV-2-infected mice while *Hsd3b7* remained unchanged (**Figure S14).** NIBR189 or vehicle was administered to C57BL/6J or *Gpr183*$^{-/-}$ mice twice daily from 24 h post-SARS-CoV-2 infection until the end of the experiment (**Figure 5a**). NIBR189-treated C57BL/6J mice lost significantly less weight and recovered faster compared to vehicle treated mice (**Figure 5b and S15**). Similarly, *Gpr183*$^{-/-}$ mice had less severe SARS-CoV-2 infection. Collectively, these data demonstrate that oxysterols are produced in the lung upon SARS-CoV-2 infection and GPR183 antagonism significantly reduced SARS-CoV-2 infection severity.

GPR183 antagonism reduces macrophage infiltration and inflammatory cytokine expression in the lung of SARS-CoV-2 infected mice

Next, we investigated whether GPR183 antagonism decreases macrophage infiltration and inflammatory cytokines in the lung. SARS-CoV-2-infected C57BL/6J mice treated with NIBR189 had significantly reduced macrophage infiltration into the lung at 2 and 5 dpi (**Figure 5c**). NIBR189 treatment was associated with reduced *Tnf, Il10* and *Ifng* mRNA expression at 2 dpi (**Figure 6a and S16**), and reduced *Tnf*, *Il1b and Il6* expression at 5 dpi (**Figure 6b and S16**). Early interferon responses were not affected by NIBR189 with comparable *Ifnb* and *Ifnl* expression at 2 dpi in C57BL/6J mice, but late interferon responses (5 dpi) were significantly lower in NIBR-treated animals compared to controls (**Figure 6b**). No differences between treatment groups were observed for mRNAs encoding *Ccl2, Il1b*, or *Il6* at 2 dpi and *Ccl2*, *Il10* and *Ifng* at 5 dpi (**Figure S16**). These results demonstrate that reduced macrophage infiltration in NIBR189-treated mice was associated with reduced pro-inflammatory cytokine expression in the lung, while the early anti-viral IFN responses remained unchanged.

GPR183 antagonism reduces SARS-CoV-2 loads

Finally, we investigated whether NIBR189 treatment is associated with altered viral loads. SARS-CoV-2 nucleocapsid protein (Np) expression was reduced in NIBR189-treated C57BL/6J mice compared to those administered vehicle at 2 dpi (**Figure 7 a,b**). Np expression was not detected at 5 dpi, when the animals recovered from the infection. However, at the mRNA level, viral *Mpro* RNA loads in the lungs of

NIBR189-treated mice were significantly lower at 5 dpi (**Figure 7c**). Corroborating this, viral PFUs were significantly lower at both 2 and 5 dpi in NIBR-treated animals (**Figure S17**). In summary, we demonstrate here that GPR183 antagonism reduces viral loads, macrophage infiltration and production of pro-inflammatory cytokines in SARS-CoV-2 infection.

Lung macrophages from COVID-19 patients upregulate *CH25H, CYP7B1, HSD3B7* and *GPR183*

To determine whether the oxysterol producing enzymes are increased in humans during SARS-CoV-2 infection we analysed scRNASeq data from healthy controls and COVID-19 patients with moderate and severe disease [12]. We found that *CH25H, CYP7B1* and *HSD3B7* were significantly upregulated in COVID-19 and almost exclusively expressed in macrophages (**Figure 8**). While *GPR183* expression increased significantly in macrophages and myeloid DCs during COVID-19, its expression remained unchanged on other immune cell types.

Discussion

We report that 25-OHC and 7α,25-OHC are produced in the lung upon IAV or SARS-CoV-2 infection attracting monocytes-macrophages in a GPR183-dependent manner. Reduced macrophage infiltration and inflammatory cytokine production in *Gpr183*$^{-/-}$ mice and NIBR189-treated C57BL/6J mice, significantly improved SARS-CoV-2 infection severity. The antagonist attenuated SARS-CoV-2, but not IAV loads. Whether this is due to pathogen-specific effects or due to more severe disease observed in the IAV model compared to the SARS-CoV-2 model, remains to be investigated. However, macrophage infiltration and inflammatory cytokine production was reduced in both viral models.

In animal models of IAV and SARS-CoV-2 myeloid cells rapidly infiltrate into the lungs [3, 4, 24]. Patients with severe COVID-19 had higher proportions of GPR183^{+} macrophages and more activated macrophages in BALF [23] strongly implicating macrophages as key contributors to COVID-19-associated hyperinflammation. BALF from severe COVID-19 patients was enriched in the chemokines CCL2 and CCL7 that recruit monocytes to the lung via the chemokine receptor CCR2 [25]. Historically, chemokines have been considered as the main drivers of immune cell migration into the lung; however, our work here reveals that oxysterols have a non-redundant role in monocyte-macrophage infiltration. We further demonstrate that lung macrophages from COVID-19 patients express higher levels of the oxysterol producing enzymes and GPR183 indicating that this mechanism is conserved in humans. Similar to our observations in *Gpr183*$^{-/-}$ mice, mice lacking CCR2 have delayed macrophage infiltration into the lung [21], however CCR2 is also required for T cell migration. Therefore, animals lacking CCR2 had delayed T cell infiltration and higher viral titres [26]. Although GPR183 is expressed on T cells it is not essential for T cell migration into the lung [27] and antagonising GPR183 did not negatively impact the T cell compartment nor other immune cell subsets.

We recently showed in a murine model of *Mycobacterium tuberculosis* (Mtb) infection that both GPR183 and the 7α,25-OHC-producing enzyme CYP7B1 are required for rapid macrophage infiltration into the lung upon mycobacterial infection [18]. In the Mtb model, GPR183 was also required for infiltration of eosinophils [14]. We identified both alveolar macrophages and infiltrating macrophages as the predominant cell type expressing CH25H and CYP7B1 upon Mtb infection [18] and corroborated this here with the scRNASeq data from COVID-19 patients.

Deletion of *Ch25h* has been previously shown to be protective in a mouse model of influenza [28]. 25-OHC was increased in a model of acute lung injury (ALI), however it was decreased in a house dust mite induced model of asthma [8]. Intra-tracheal administration of 25-OHC improved inflammatory markers in the ALI model, whereas it worsened the hallmarks of the asthma model. In both models *Gpr183* expression was unaffected. This suggests that 25-OHC production is model specific.

Here we show that reduced macrophage infiltration in *Gpr183*$^{-/-}$ mice and NIBR189-treated C57BL/6J mice was associated with reduced pro-inflammatory cytokine production, likely due to lower numbers of macrophages present in the tissue. Although we did not observe a NIBR189-mediated reduction in *Tnf*, *Il6* or *Ifnb* expression in IAV-infected or LPS-stimulated BMDMs (**Figure S18**), we cannot completely exclude a direct effect of NIBR189 on cytokine production by other immune cells. Irrespective of the exact mechanism, lower pro-inflammatory cytokine production in NIBR189-treated animals may explain, at least in part, the better disease outcomes.

While pro-inflammatory cytokines can be detrimental to the host [30], early type I and III IFNs are crucial in controlling viral replication during IAV [31, 32] and SARS-CoV-2 infection [33, 34]. NIBR189 did not alter early type I or III IFN responses in SARS-CoV-2-infected animals, suggesting that the anti-viral response was not impaired by the treatment.

Several oxysterols can have a direct anti-viral effect [9]. CH25H/25-OHC have been shown to inhibit SARS-CoV-2 infection *in vitro* by blocking the virus-host cell membrane fusion [36, 37]. Whether NIBR189, which is structurally different from oxysterols, affects viral entry/replication remains to be elucidated.

Other immunosuppressive therapies used in severe COVID-19 like glucocorticoids increase ACE2 expression which promotes viral entry/replication [38, 39] and delays SARS-CoV-2 clearance [40]. NIBR189 did not increase *Ace2* mRNA (**Figure S19**), but *Ace2* expression was downregulated to lesser extent in NIBR189-treated animals, which is consistent with lower viral loads.

In summary, we provide the first preclinical evidence of GPR183 as a novel host target for therapeutic intervention to reduce macrophage-mediated hyperinflammation, SARS-CoV-2 loads and COVID-19 severity.

Author contributions

Conceptualization: CXF, SB, MJS, KRS, MMR, KR Methodology: KYC, HBO, BJA, BM, SR Investigation: CXF, SB, KYC, MDN, HBO, BJA, BM, SR, RW, CS, LB, KB, SS, JES, RP, YY, JPL AK Writing-original draft: CXF, SB, KR Writing-review and editing: all authors. Funding acquisition: SB, KRS, MMR, KR.

Acknowledgements

This study was supported by grants to KR from the Mater Foundation, the Australian Respiratory Council, Diabetes Australia, the Australian Infectious Diseases Research Centre. SB was supported by an early career seed grant from the Mater Foundation. The Translational Research Institute is supported by a grant from the Australian Government. The Danish Council for Independent Research I Medical Sciences supported MMR. MJS, KRS and JPL are supported by a National Health and Medical Research Council of Australia Investigator grant (1194406), Investigator Grant (2007919) and Senior Research Fellowship (1136130) respectively. We thank the Queensland Health Forensic and Scientific Services, Queensland Department of

Health, for providing SARS-CoV-2 isolate. We thank A/Prof Sumaira Hasnain for sharing antibodies used in this study. We acknowledge the technical assistance of the team that operates and maintains the Australian Galaxy service (https://usegalaxy.org.au/). We thank Profs David Hume, Maher Gandhi, and Dr Jake Gratten from the Mater Research Institute – The University of Queensland for critical review of the manuscript.

References

1. Flerlage T, Boyd DF, Meliopoulos V, et al. Influenza virus and SARS-CoV-2: pathogenesis and host responses in the respiratory tract. *Nat Rev Microbiol* 2021: 19(7): 425-441.

2. Chen ST, Park MD, Del Valle DM, et al. Shift of lung macrophage composition is associated with COVID-19 disease severity and recovery. *bioRxiv* 2022.

3. Speranza E, Williamson BN, Feldmann F, et al. Single-cell RNA sequencing reveals SARS-CoV-2 infection dynamics in lungs of African green monkeys. *Sci Transl Med* 2021: 13(578).

4. Singh DK, Aladyeva E, Das S, et al. Myeloid cell interferon responses correlate with clearance of SARS-CoV-2. *Nat Commun* 2022: 13(1): 679.

5. Shen ZJ, Hu J, Kashi VP, et al. Epstein-Barr Virus-induced Gene 2 Mediates Allergen-induced Leukocyte Migration into Airways. *Am J Respir Crit Care Med* 2017: 195(12): 1576-1585.

6. Jia J, Conlon TM, Sarker RS, et al. Cholesterol metabolism promotes B-cell positioning during immune pathogenesis of chronic obstructive pulmonary disease. *EMBO Mol Med* 2018: 10(5).

7. Sugiura H, Koarai A, Ichikawa T, et al. Increased 25-hydroxycholesterol concentrations in the lungs of patients with chronic obstructive pulmonary disease. *Respirology* 2012: 17(3): 533-540.

8. Bottemanne P, Paquot A, Ameraoui H, et al. 25-Hydroxycholesterol metabolism is altered by lung inflammation, and its local administration modulates lung inflammation in mice. *FASEB J* 2021: 35(4): e21514.

9. Foo CX, Bartlett S, Ronacher K. Oxysterols in the Immune Response to Bacterial and Viral Infections. *Cells* 2022: 11(2).

10. Mutemberezi V, Guillemot-Legris O, Muccioli GG. Oxysterols: From cholesterol metabolites to key mediators. *Prog Lipid Res* 2016: 64: 152-169.

11. Hannedouche S, Zhang J, Yi T, et al. Oxysterols direct immune cell migration via EBI2. *Nature* 2011: 475(7357): 524-527.

12. Liu C, Yang XV, Wu J, et al. Oxysterols direct B-cell migration through EBI2. *Nature* 2011: 475(7357): 519-523.

13. Emgard J, Kammoun H, Garcia-Cassani B, et al. Oxysterol Sensing through the Receptor GPR183 Promotes the Lymphoid-Tissue-Inducing Function of Innate Lymphoid Cells and Colonic Inflammation. *Immunity* 2018: 48(1): 120-132 e128.

14. Bohrer AC, Castro E, Tocheny CE, et al. Rapid GPR183-mediated recruitment of eosinophils to the lung after Mycobacterium tuberculosis infection. 2022: 2022.2002.2018.480919.

15. Spann NJ, Glass CK. Sterols and oxysterols in immune cell function. *Nat Immunol* 2013: 14(9): 893-900.

16. Preuss I, Ludwig MG, Baumgarten B, et al. Transcriptional regulation and functional characterization of the oxysterol/EBI2 system in primary human macrophages. *Biochem Biophys Res Commun* 2014: 446(3): 663-668.

17. Gessier F, Preuss I, Yin H, et al. Identification and characterization of small molecule modulators of the Epstein-Barr virus-induced gene 2 (EBI2) receptor. *J Med Chem* 2014: 57(8): 3358-3368.

18. Ngo MD, Bartlett S, Bielefeldt-Ohmann H, et al. A blunted GPR183/oxysterol axis during dysglycemia results in delayed recruitment of macrophages to the lung during M. tuberculosis infection. *J Infect Dis* 2022.

19. Bartlett S, Gemiarto AT, Ngo MD, et al. GPR183 Regulates Interferons, Autophagy, and Bacterial Growth During Mycobacterium tuberculosis Infection and Is Associated With TB Disease Severity. *Front Immunol* 2020: 11: 601534.

20. Pereira JP, Kelly LM, Xu Y, et al. EBI2 mediates B cell segregation between the outer and centre follicle. *Nature* 2009: 460(7259): 1122-1126.

21. Poczobutt JM, Gijon M, Amin J, et al. Eicosanoid profiling in an orthotopic model of lung cancer progression by mass spectrometry demonstrates selective production of leukotrienes by inflammatory cells of the microenvironment. *PLoS One* 2013: 8(11): e79633.

22. Zhou JH, Wang YN, Chang QY, et al. Type III Interferons in Viral Infection and Antiviral Immunity. *Cell Physiol Biochem* 2018: 51(1): 173-185.

23. Liao M, Liu Y, Yuan J, et al. Single-cell landscape of bronchoalveolar immune cells in patients with COVID-19. *Nat Med* 2020: 26(6): 842-844.

24. Corry J, Kettenburg G, Upadhyay AA, et al. Infiltration of inflammatory macrophages and neutrophils and widespread pyroptosis in lung drive influenza lethality in nonhuman primates. *PLoS Pathog* 2022: 18(3): e1010395.

25. Zhou Z, Ren L, Zhang L, et al. Heightened Innate Immune Responses in the Respiratory Tract of COVID-19 Patients. *Cell Host Microbe* 2020: 27(6): 883-890 e882.

26. Dawson TC, Beck MA, Kuziel WA, et al. Contrasting effects of CCR5 and CCR2 deficiency in the pulmonary inflammatory response to influenza A virus. *Am J Pathol* 2000: 156(6): 1951-1959.

27. Hoft SG, Sallin MA, Kauffman KD, et al. The Rate of CD4 T Cell Entry into the Lungs during Mycobacterium tuberculosis Infection Is Determined by Partial and Opposing Effects of Multiple Chemokine Receptors. *Infect Immun* 2019: 87(6).

28. Gold ES, Diercks AH, Podolsky I, et al. 25-Hydroxycholesterol acts as an amplifier of inflammatory signaling. *Proc Natl Acad Sci U S A* 2014: 111(29): 10666-10671.

29. Del Valle DM, Kim-Schulze S, Huang HH, et al. An inflammatory cytokine signature predicts COVID-19 severity and survival. *Nat Med* 2020: 26(10): 1636-1643.

30. Diamond MS, Kanneganti TD. Innate immunity: the first line of defense against SARS-CoV-2. *Nat Immunol* 2022: 23(2): 165-176.

31. Stanifer ML, Guo C, Doldan P, et al. Importance of Type I and III Interferons at Respiratory and Intestinal Barrier Surfaces. *Front Immunol* 2020: 11: 608645.

32. Galani IE, Triantafyllia V, Eleminiadou EE, et al. Interferon-lambda Mediates Non-redundant Front-Line Antiviral Protection against Influenza Virus Infection without Compromising Host Fitness. *Immunity* 2017: 46(5): 875-890 e876.

33. Lokugamage KG, Hage A, de Vries M, et al. Type I interferon susceptibility distinguishes SARS-CoV-2 from SARS-CoV. *bioRxiv* 2020.

34. Vanderheiden A, Ralfs P, Chirkova T, et al. Type I and Type III Interferons Restrict SARS-CoV-2 Infection of Human Airway Epithelial Cultures. *J Virol* 2020: 94(19).

35. Cameron MJ, Ran L, Xu L, et al. Interferon-mediated immunopathological events are associated with atypical innate and adaptive immune responses in patients with severe acute respiratory syndrome. *J Virol* 2007: 81(16): 8692-8706.

36. Wang S, Li W, Hui H, et al. Cholesterol 25-Hydroxylase inhibits SARS-CoV-2 and other coronaviruses by depleting membrane cholesterol. *EMBO J* 2020: 39(21): e106057.

37. Zang R, Case JB, Yutuc E, et al. Cholesterol 25-hydroxylase suppresses SARS-CoV-2 replication by blocking membrane fusion. *Proc Natl Acad Sci U S A* 2020: 117(50): 32105-32113.

38. Sinha S, Cheng K, Schaffer AA, et al. In vitro and in vivo identification of clinically approved drugs that modify ACE2 expression. *Mol Syst Biol* 2020: 16(7): e9628.

39. Saheb Sharif-Askari N, Saheb Sharif-Askari F, Alabed M, et al. Effect of Common Medications on the Expression of SARS-CoV-2 Entry Receptors in Kidney Tissue. *Clin Transl Sci* 2020: 13(6): 1048-1054.

40. Li J, Liao X, Zhou Y, et al. Association between glucocorticoids treatment and viral clearance delay in patients with COVID-19: a systematic review and meta-analysis. *BMC Infect Dis* 2021: 21(1): 1063.

Figures

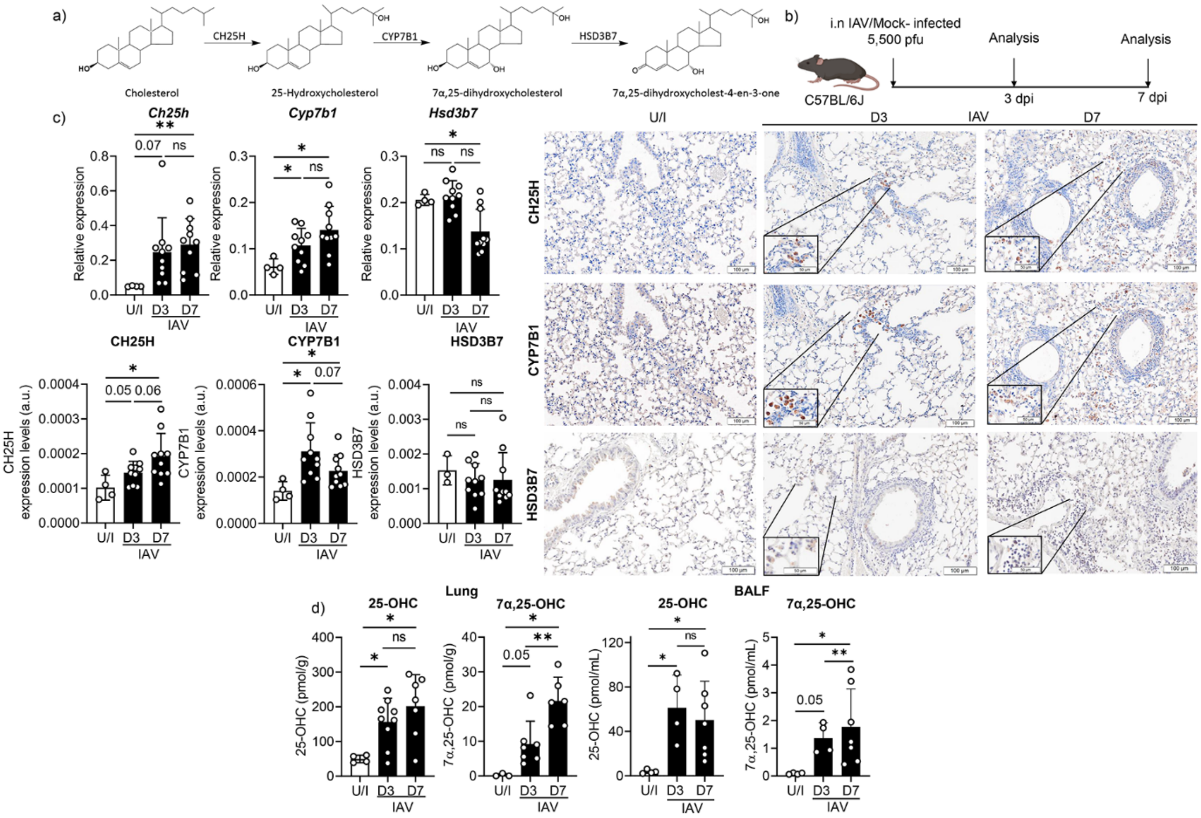

Figure 1. IAV infection leads to upregulation of CH25H and CYP7B1 expression in the lung and production of the oxysterols 25-OHC and 7α,25-OHC

a) The biosynthetic pathway of 25-OHC and 7α,25-OHC. b) Experimental design; C57BL/6J mice were infected intranasally with 5,500 PFU of IAV and mRNA expression of c) *Ch25h, Cyp7b1* and *Hsd3b7* were measured by qRT-PCR at 3 dpi and 7 dpi normalised to *Hprt* (upper panel). Quantitative analysis of CH25H, CYP7B1 and HSD3B7 protein labelling by IHC (lower panel). Representative IHC images of CH25H, CYP7B1 and HSD3B7 in lung sections of uninfected or IAV-infected mice. d) Concentrations of 25-OHC and 7α,25-OHC in the lungs at 3 dpi and 7 dpi expressed in pmol per gram lung tissue (left panel) or in pmol per mL BALF (right). Data are presented as mean ± SD of n=4 uninfected and n=6-10 infected mice per timepoint.

Scale Bar = 100μm; dpi = days post-infection; U/I = mock infected; ns., not significant; *, $P < 0.05$; **, $P < 0.01$ indicate significant differences.

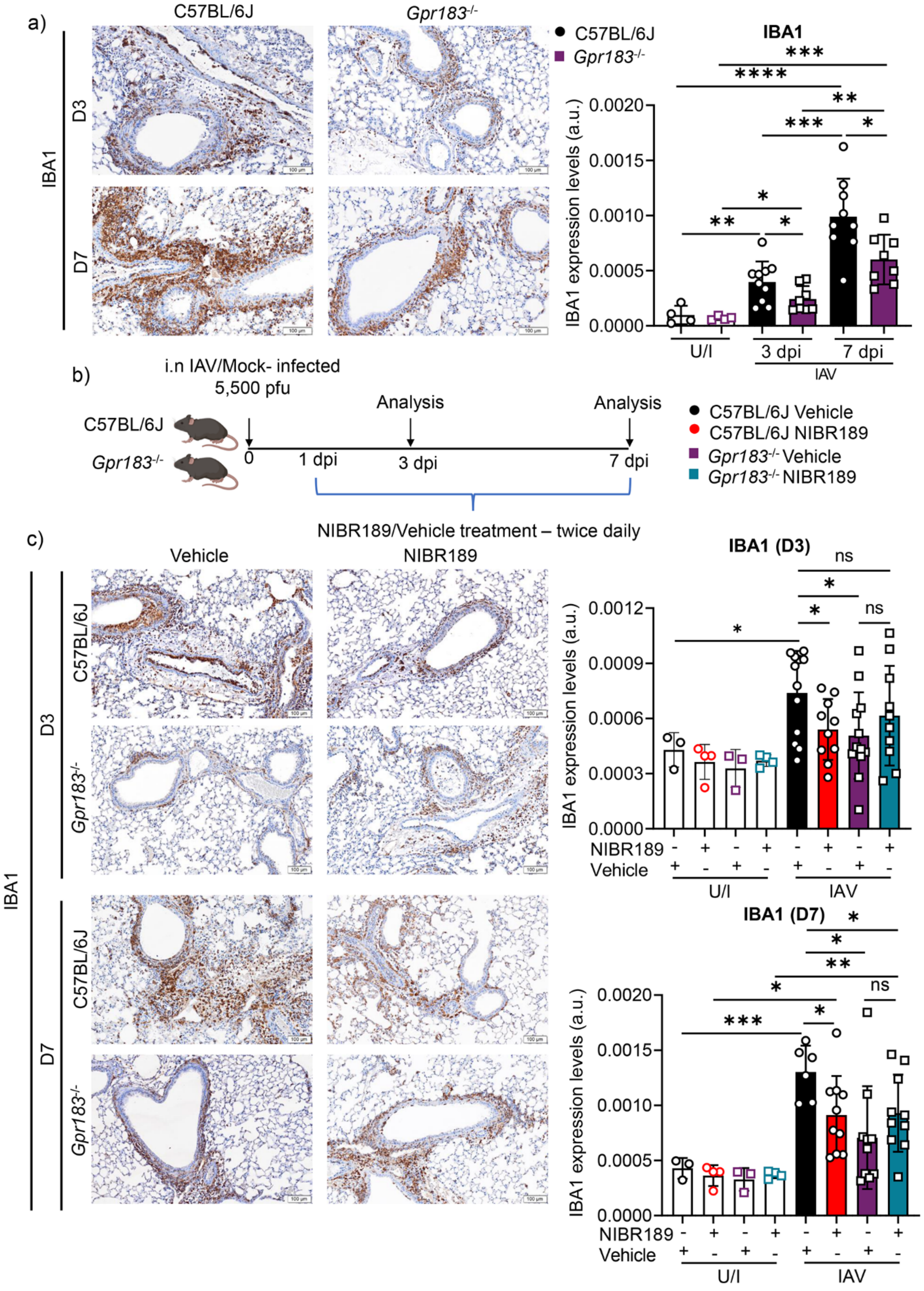
a)
C57BL/6J
Gpr183-/-
IBA1
D3
D7
● C57BL/6J
■ Gpr183-/-
IBA1
IBA1 expression levels (a.u.)
0.0020
0.0015
0.0010
0.0005
0.0000
U/I
3 dpi
7 dpi
IAV
****
***
**
*
b)
i.n IAV/Mock- infected
5,500 pfu
C57BL/6J
Gpr183-/-
0
1 dpi
Analysis
3 dpi
Analysis
7 dpi
NIBR189/Vehicle treatment – twice daily
● C57BL/6J Vehicle
● C57BL/6J NIBR189
■ Gpr183-/- Vehicle
■ Gpr183-/- NIBR189
c)
Vehicle
NIBR189
IBA1
D3
D7
C57BL/6J
Gpr183-/-
IBA1 (D3)
IBA1 expression levels (a.u.)
0.0012
0.0009
0.0006
0.0003
0.0000
NIBR189 - + - + - + - +
Vehicle + - + - + - + -
U/I
IAV
ns
*
IBA1 (D7)
0.0020
0.0015
0.0010
0.0005
0.0000
***
**
*
ns

Figure 2. Deletion of the *Gpr183* gene or administration of a GPR183 antagonist reduces macrophage infiltration in IAV-infected lungs. C57BL/6J and *Gpr183*$^{-/-}$ mice were infected intranasally with 5,500 PFU of IAV. a) Representative IHC images of IBA1 in lung sections of IAV-infected C57BL/6J and *Gpr183*$^{-/-}$ mice. Quantitative analysis of IBA1 staining. b) Experimental design; C57BL/6J mice and *Gpr183*$^{-/-}$ mice were infected intranasally with 5,500 PFU of IAV. Mice were subsequently treated orally with 7.6 mg/kg NIBR189 or vehicle control twice daily from 1 dpi until the end of the experiment. c) Representative IHC images of IBA1 in lung sections of C57BL/6J and *Gpr183*$^{-/-}$ mice with the respective treatment groups at 3 dpi and 7 dpi. Quantitative analysis of IBA1 staining. Data are presented as mean ± SD of n = 6-12 infected mice per genotype and timepoint. dpi = days post-infection; Scale Bar = 100μm; U/I = mock infected ns = not significant; *, $P < 0.05$; **, $P < 0.01$; ***, $P < 0.001$ indicate significant differences.

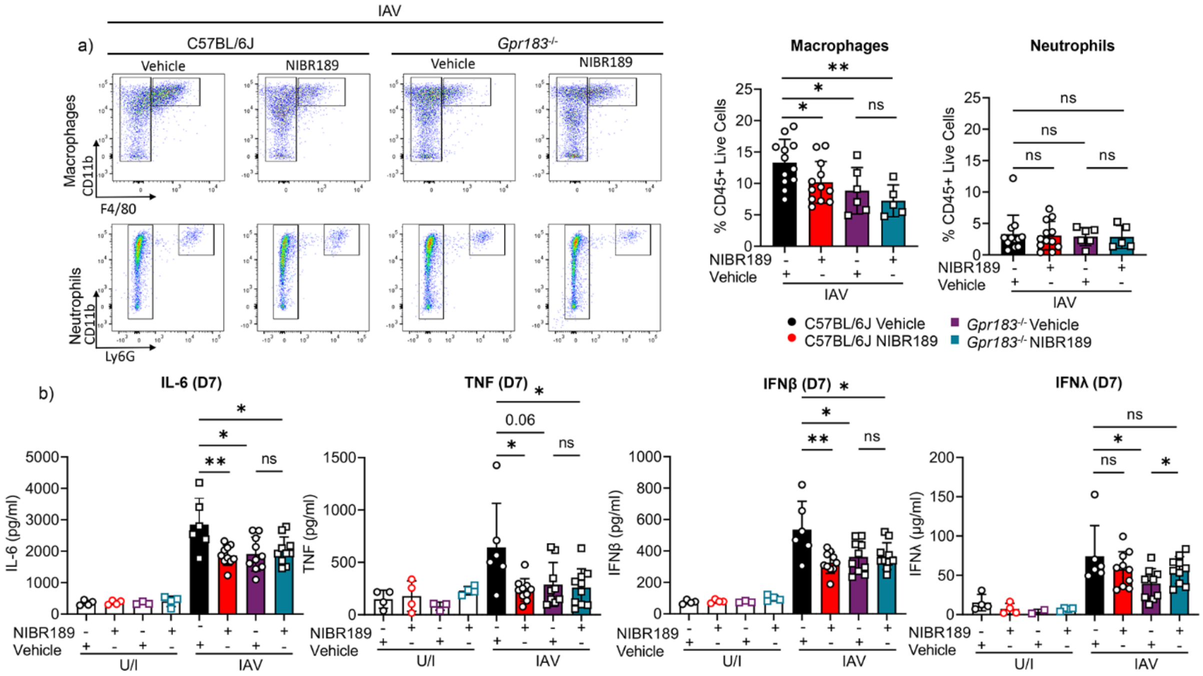

Figure 3. The GPR183 antagonist NIBR189 reduces macrophage infiltration and inflammatory cytokine production. C57BL/6J and *Gpr183*$^{-/-}$ mice were infected intranasally with 5,500 PFU of IAV. Mice were subsequently treated orally with 7.6 mg/kg NIBR189 or vehicle control twice daily from 1 dpi until the end of the experiment. a) Frequency of infiltrating macrophages (F480^{high}/CD11b^{+}/Ly6G^{-}/SigF^{-}) and neutrophils (B220^{-}CD3^{-}Ly6G^{+}) was determined by flow cytometry relative to total viable CD45^{+} immune cells at 3 dpi. Graphs show the frequency of macrophages and neutrophils. b) Cytokine measurements of IL-6, TNF, IFNβ and IFNλ at 7 dpi measured by ELISA. Data are presented as mean ± SD of n=5-12 infected mice per genotype and timepoint. dpi = days post-infection; U/I = mock infected; ns = not significant; *, $P < 0.05$; **, $P<0.01$ indicate significant differences.

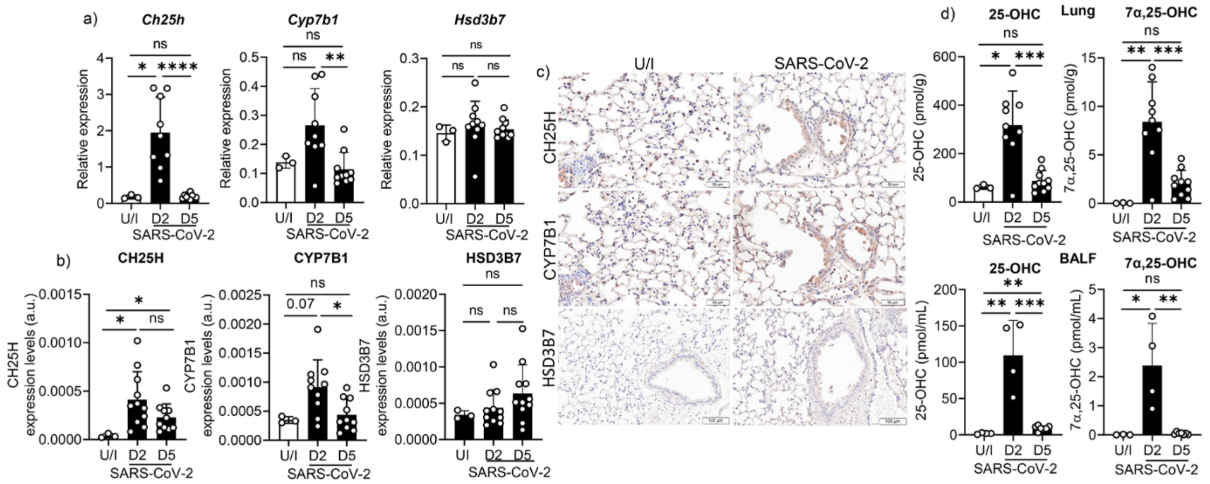

Figure 4. SARS-CoV-2 infection leads to upregulation of CH25H and CYP7B1 expression in the lung and production of the oxysterols 25-OHC and 7α,25-OHC. C57BL/6J mice were infected intranasally with approximately 8x10^4 PFU of mouse-adapted SARS-CoV-2. mRNA expression of a) *Ch25h*, *Cyp7b1* and *Hsd3b7* was measured by qRT-PCR at 2 dpi and 5 dpi normalised to *Hprt*. b) Quantitative analysis of CH25H, CYP7B1 and HSD3B7 protein by IHC labelling and c) representative IHC images of CH25H, CYP7B1 and HSD3B7 in lung sections in uninfected mice and 2 and 5 dpi. d) Concentrations of 25-OHC and 7a,25-OHC in the lungs at 2 dpi and 5 dpi expressed in pmol per gram lung tissue (top panel) or in pmol per mL BALF (bottom panel). Data are presented as mean ± SD of n=3 uninfected mice and n= 9-10 infected mice per timepoint. Scale Bar = 50μm; U/I = mock infected; dpi = days post-infection; ns = not significant; *, $P < 0.05$; **, $P < 0.01$; ***, $P < 0.001$; ****, $P < 0.0001$ indicate significant differences.

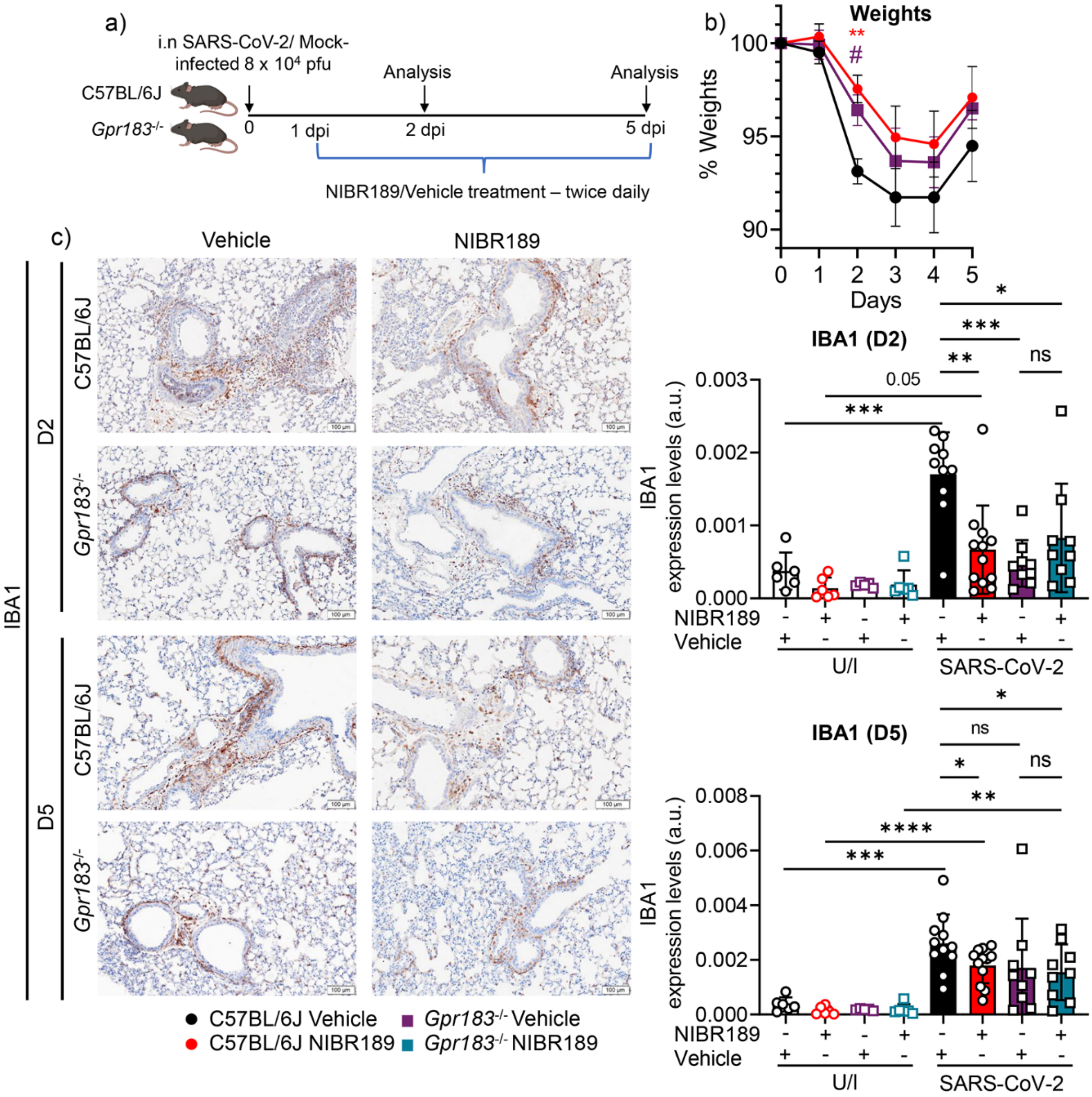

Figure 5. GPR183 antagonism resulted in less SARS-CoV-2 infection-induced weight loss and in reduced macrophage infiltration. C57BL/6J and *Gpr183*$^{-/-}$ mice were infected intranasally with approximately 8x10^4 PFU of mouse-adapted SARS-CoV-2. Mice were subsequently treated orally with 7.6 mg/kg NIBR189 or vehicle control twice daily from 1 dpi until the end of the experiment. a) Experimental design; b) Weights of mice displayed as percentage of the weight at time of inoculation. c) Representative IHC images of IBA1 in lung of C57BL/6J and *Gpr183*$^{-/-}$ mice with the respective treatment groups at 2 dpi and 5 dpi (left). Scale Bar = 100µm. Quantitative

analysis of IBA1 (right). Data are presented as mean ± SD of n=9-12 infected mice per genotype and timepoint. Scale Bar = 100µm; U/I uninfected; dpi = days post-infection; ns = not significant; *, $P < 0.05$; **, $P < 0.01$; ***, $P < 0.001$ indicate significant differences.

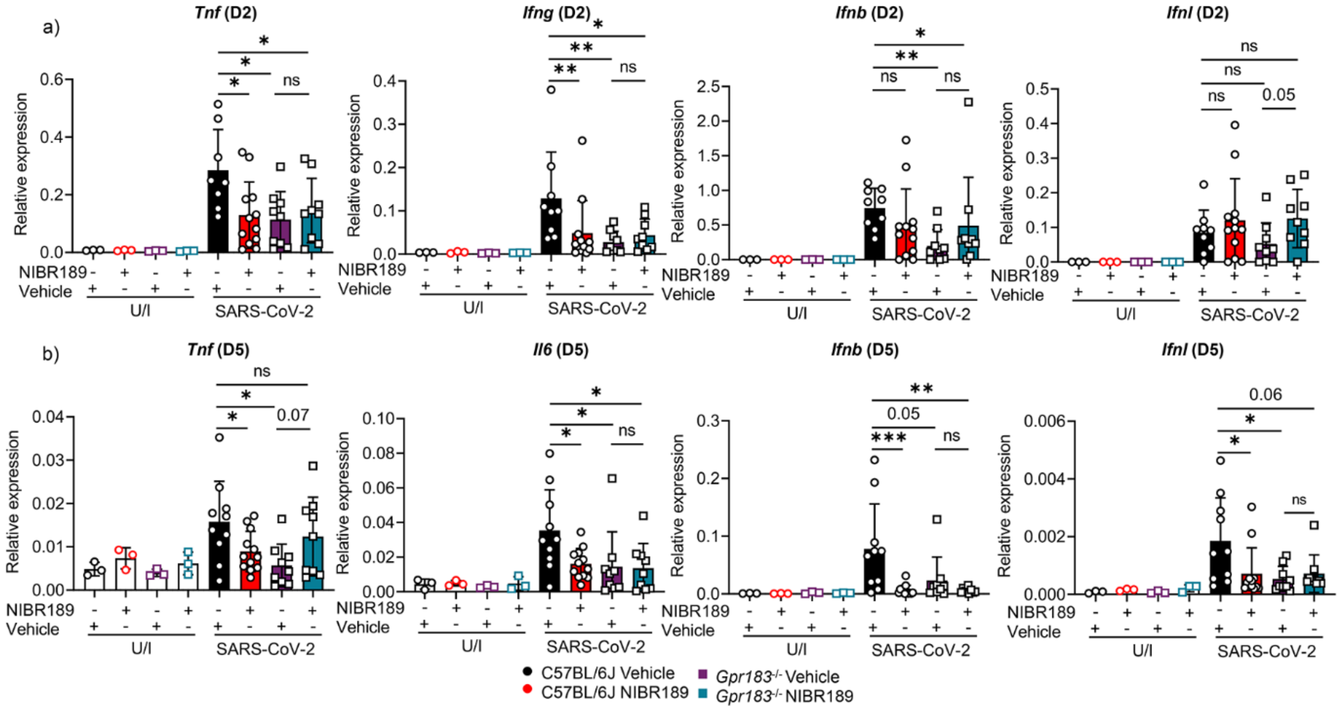

Figure 6. GPR183 antagonism led to reduced inflammatory cytokine profile. C57BL/6J and *Gpr183*$^{-/-}$ mice were infected intranasally with approximately 8x10^{4} PFU of mouse-adapted SARS-CoV-2. Mice were subsequently treated orally with 7.6 mg/kg NIBR189 or vehicle control twice daily from 1 dpi until the end of the experiment. Relative expression of a) *Tnf*, *Ifng, Ifnb and Ifnl* at 2 dpi and b) *Tnf*, *Il6, Ifnb and Ifnl* at 5 dpi in the lungs measured by RT-qPCR, normalised to *Hprt*. Data are presented as mean ± SD of n=3 uninfected mice and n= 9-12 infected mice per genotype and timepoint. U/I = mock infected; dpi = days post-infection; ns = not significant; *, $P < 0.05$; **, $P < 0.01$; ***, $P < 0.001$ indicate significant differences.

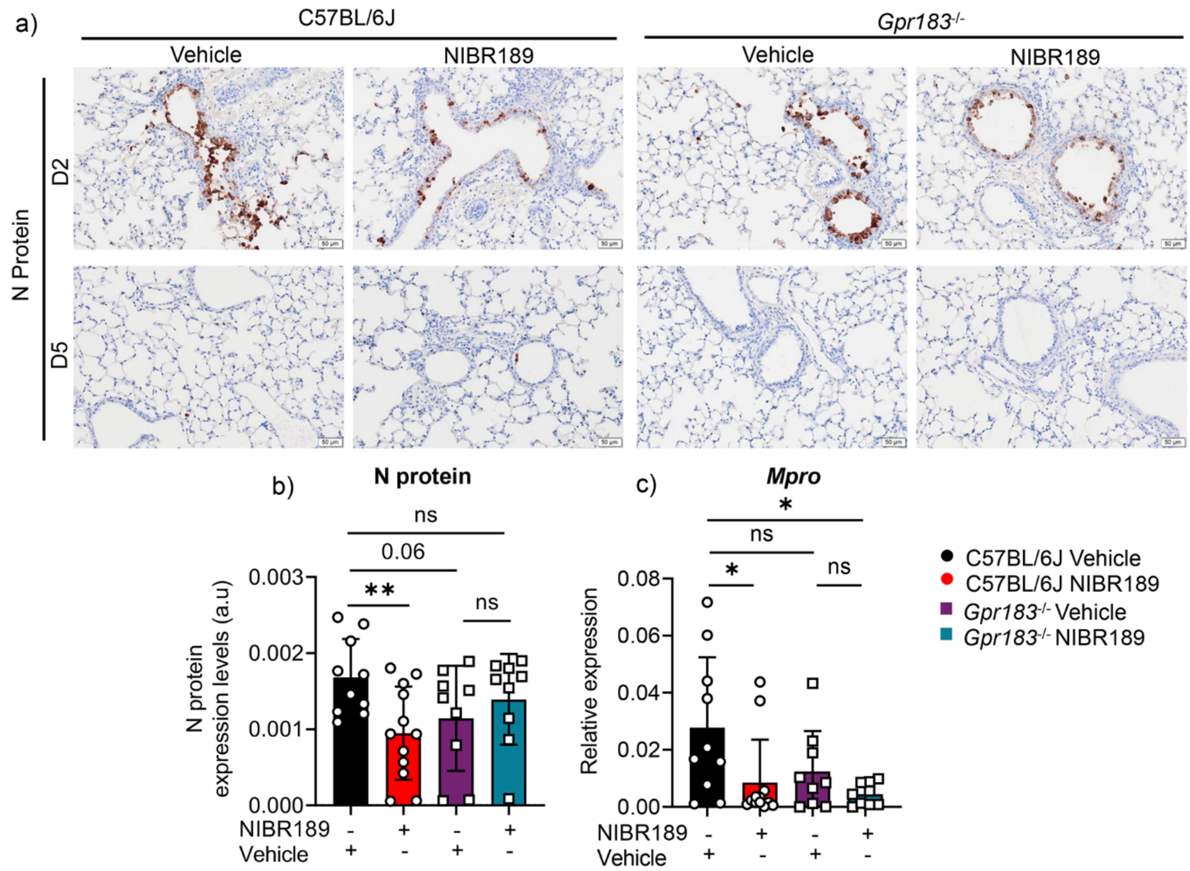

Figure 7. Mice treated with GPR183 antagonist had lower SARS-CoV-2 loads.

C57BL/6J and *Gpr183*$^{-/-}$ mice were infected intranasally with approximately $8x10^4$ PFU of mouse-adapted SARS-CoV-2. Mice were subsequently treated orally with 7.6 mg/kg NIBR189 or vehicle control twice daily from 1 dpi until the end of the experiment. a) Representative IHC images of viral nucleocapsid (Np) expression at 2 dpi and 5 dpi. b) Quantitative analysis of viral Np expression of the treatment groups at 2 dpi. c) Viral load was assessed in the lung through the detection of *Mpro* RNA by RT-qPCR at 5 dpi, normalised to HPRT. Data are presented as mean ± SD of n=9-12 infected mice per genotype and timepoint. Scale Bar = 50µm; U/I = mock infected; dpi = days post-infection; ns = not significant; *, $P < 0.05$; **, $P < 0.01$, indicate significant differences.

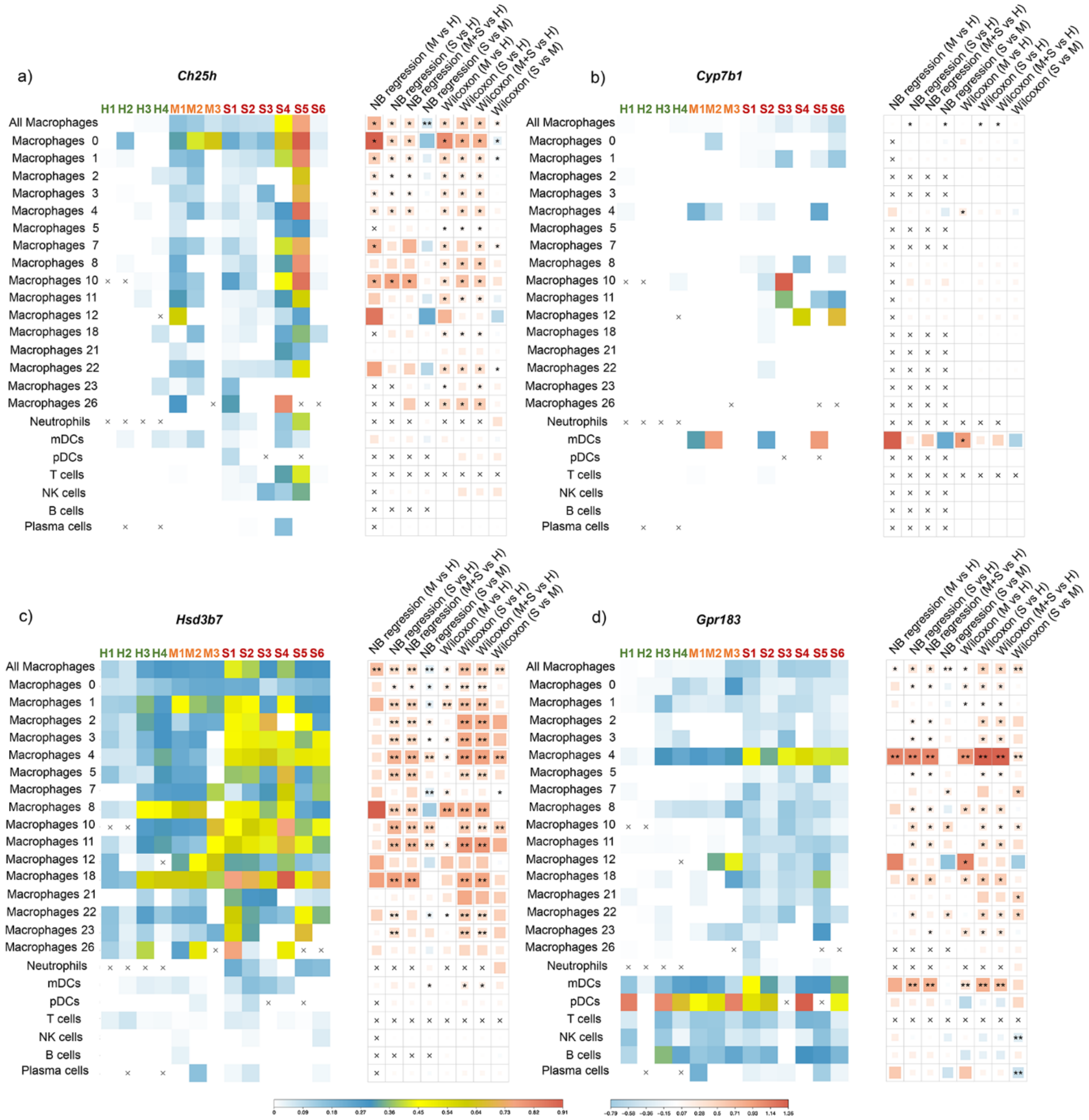

Figure 8. Single cell RNASeq expression analysis of cells collected by bronchoalveolar lavage from healthy controls and COVID19 patients. Summary heatmap (left panels) showing average normalised expression level of gene a) *Ch25h* b) *Cyp7b1,* c) *Hsd3b7* and d) *Gpr183* per individual per cell type cluster. Summary heatmap (right panels) show the average log fold change (logFC) in expression of each gene in 24 cell type clusters between: (1) moderate COVID-19 cases ("M") and healthy controls ("H"); (2) severe COVID-19 cases ("S") and healthy controls; (3) COVID-19

cases (“M&S””) and healthy controls; and (4) severe and moderate COVID-19 cases, respectively. The logFC values were estimated using (1) negative binomial generalised linear models applied to raw UMI counts, adjusting for total UMI counts per cell, number of genes detected per cell and percent mitochondrial counts per cell (“NB regression”); or (2) non-parametric Wilcoxon rank sum test applied to normalised counts. Significant associations are highlighted with a single asterisk if they surpass Bonferroni significance ($p < 1.30\times10-4$) or a double asterisk if they were further expressed in at least 5% of cells in both groups with an absolute value of logFC greater than 0.25. A logFC greater than zero suggests the expression level of the gene is higher among the focal group (e.g., moderate COVID-19 cases) compared to the other group (e.g., healthy controls), or vice versa.

Online Data Supplement

GPR183 antagonism reduces macrophage infiltration in influenza and SARS-CoV-2 infection

Cheng Xiang Foo[1#], Stacey Bartlett[1#], Keng Yih Chew[2,] Minh Dao Ngo[1], Helle Bielefeldt-Ohmann[2,3], Buddhika Jayakody Arachchige[4], Benjamin Matthews[4], Sarah Reed[4], Ran Wang[1], Christian Smith[1], Matthew J. Sweet[3,5], Lucy Burr[6], Kavita Bisht[1], Svetlana Shatunova[1], Jane E. Sinclair[2], Rhys Parry[2], Yuanhao Yang[1], Jean-Pierre Lévesque[1], Alexander Khromykh[2,3], Mette Marie Rosenkilde[7], Kirsty R. Short[2,3], and Katharina Ronacher[1,3*]

Methods

Mouse models

IAV infected mice were sacrificed at 3 dpi and 7 dpi for examination. SARS-CoV-2 infected mice were sacrificed at 2 dpi and 5 dpi. Lungs were homogenised in DMEM for use in plaque assays and ELISAs. For RNA processing, lungs were collected in TRIzol (Invitrogen). For oxysterol extractions, lungs and BAL fluid were collected in methanol. For histological analysis the lungs were fixed in 10% neutral buffered formalin.

Mouse-adapted SARS-CoV-2 strain

Six x 10^4 PFU of B1.351 was administrated intranasally to ketamine-anesthetized mice. Mice were monitored daily for weight loss and clinical signs of disease severity. Four days after inoculation, mice were euthanised, and bronchoalveolar lavage (BAL) was performed. The bronchoalveolar lavage fluid (BALF) was subsequently pooled and used to intranasally inoculate a new batch of mice. The process was repeated until a virulent phenotype of the virus was observed as determined by weight loss and clinical signs, which happened after four passages. To determine whether the mouse adapted SARS-CoV-2 acquired mutations sequencing of viral RNA was performed. Briefly, viral RNA was extracted from BALF using the Qiagen Mini kit and the quality confirmed suing the Agilent Bioanalyzer with 210 Expert software. Library preparations were performed using the Illumina Stranded Total RNA Ribo Zero Plus kit. Sequencing was performed using the NextSeq Midoutput kit, 125bp paired-end configuration with 19-25 million reads per sample. Sequencing analysis was executed using Galaxy software. Whole-genome sequencing revealed a C to T mutation in position 10804 of the SARS-CoV-2 Beta genome resulting in the NSP5 mutation P252L. This mutation was rapidly selected from 3.4% in the initial virus stock to 8.8% in passage one. From passage two, this mutation reached consensus (60%) and underwent further fixation in passage three at 87% to final frequency of 92% in passage four. A mutation in NSP5 was detected in this mouse adapted SARS-CoV-2 strain (Figure S1).

BALF of the mice from the fourth passage was subsequently pooled and used to inoculate Vero E6 cells for propagation, creating the viral stocks for our mouse-adapted strain. To verify the virulent phenotype of the mouse-adapted virus was retained after propagation in Vero E6 cells, the cell grown virus was used to inoculate a new batch of mice. The same viral stock was used to infect mice with $8x10^4$ PFU for the experiments described.

Bioinformatic analysis of mouse-adapted SARS-CoV-2 sequence data

Base-called fastq files were mapped to the QLD1520 SARS-CoV-2 isolate (GISAID accession EPI_ISL_968081) using Bowtie2 (v2.4.2) [1] under default alignment conditions. Sub consensus variants of alignment files were identified using iVar (v1.2.2) [2] with a minimum quality score threshold of 20 and depth of 5000. Coverage of mapped alignment files was determined using samtools (v1.3) depth. Frequencies and coverage of variant positions were manually validated using Integrative Genomics Viewer (Version: 2.7.0) [3]. Variant frequencies and alignment depth was visualised using GraphPad Prism (v9.3.1). Raw fastq data generated in this study have been deposited in the Sequence Read Archive hosted by the National Center for Biotechnology Information with accession number PRJNA849351.

BALF collection

Mice were euthanised before performing the BAL procedure. A lavage was performed by injection of 750 µL of PBS supplemented with 2mM EDTA 2mM and 0.5% FBS into the trachea through a cannula. The BAL fluid was subsequently recovered from the lungs and the recovered volume recorded. The BALF was centrifuged at 400 g for 5 minutes. The supernatant was collected and stored in methanol at −80°C for oxysterol extractions. To the cell pellet, 500uL of TRIZol reagent was added for RNA extraction.

Plaque assays

IAV plaque assays were carried out on confluent monolayers of MDCK cells as previously described [4]. SARS-CoV-2 plaque assays were carried out on Vero E6 cells as described previously [5].

Oxysterol extraction from lung tissues and BAL fluid

Lung lobes from IAV and SARS-CoV-2-infected mice were homogenised in methanol. 500 µL of methanol was added to BAL fluid from IAV and SARS-CoV-2-infected mice. Oxysterols were extracted using a 1:1 dichloromethane:methanol solution containing 50 µg/mL BHT in a 30°C ultrasonic bath. Tubes were flushed with nitrogen to displace oxygen, sealed with a polytetrafluoroethylene (PTFE)-lined screw cap, and incubated at 30°C in the ultrasonic bath for 10 mins. Following centrifugation (3,500 rpm, 5 min, 25°C), the supernatant from each sample was decanted into a new tube. For liquid-liquid extraction, Dulbecco's phosphate-buffered saline (DPBS) was added to the supernatant, agitated, and centrifuged at 3,500 rpm for 5 mins at 25°C. The organic layer was recovered and evaporated under nitrogen using a 27-port drying manifold (Pierce; Fisher Scientific, Fair Lawn, NJ). Oxysterols were isolated by solid-phase extraction (SPE) using 200 mg, 3 mL aminopropyl SPE columns (Biotage; Charlotte, NC). The samples were dissolved in 1 ml of hexane and transferred to the SPE column, followed by a rinse with 1 ml of hexane to elute nonpolar compounds. Oxysterols were eluted from the column with 4.5 ml of a 23:1 mixture of chloroform: methanol and dried under nitrogen. Samples were resuspended in 50µl of warm (37°C) 90% methanol with 0.1% DMSO, and placed in an ultrasonic bath for 5 min at 30°C. A standard curve was extracted for 25-OHC (Sigma-Aldrich, H1015) and 7α,25-OHC (SML0541, Sigma-Aldrich) using the above method. Dichloromethane, butylated hydroxytoluene (BHT) and hexane were purchased from Sigma-Aldrich.

Mass spectrometric quantitation of 25-OHC and 7α,25-OHC in lung homogenates

Samples were analysed on an AB Sciex QTRAP® 5500 (ABSCIEX, Redwood City, CA) mass spectrometer coupled to a Shimadzu Nexera2 UHPLC. A Kinetex Pentafluorophenyl (PFP) column (100 × 2.1mm, 1.7µM, 1000A, Phenomenex) was used for the separation of 25-OHC and 7α,25-OHC from other oxysterols. Mobile phase used for separation were, A - 0.1% formic acid with water and B - 100% acetonitrile with 0.1% formic acid. Five µL of sample were loaded at 0.5 mL/min and separated using linear gradient with increasing percentage of acetonitrile. Samples were washed for 1.3 min after loading with 30% mobile phase B followed by linear gradient of 30% - 70% over 9 min and 70% to 99% over 1 min. The column was washed with 99% mobile phase B for 2 min followed by equilibration with 30% B 2 min before next injection. Column oven and auto-sampler were operated at 50°C and 15°C, respectively. Elution of analytes from the column was monitored in positive ion mode (ESI) with multiple reaction monitoring on ABSciex QTRAP® mass spectrometer equipped with Turbo spray ion source, which was operated at temp 550°C, ion spray voltage of 5500 V, curtain gas (CUR) of 30 psi, ion source gas1 (GS1) of 65 psi and ion source gas 2 (GS2) of 50 psi. Quadrupole 1 and 3 were operated at unit mass resolution at all time during the experiment. MRM pairs 385.3 > 367.3, 385 >133, 385.3 > 147.1 were monitored for 25-OHC and for 7α,25-OHC following MRM pairs were used 383.2 > 365.3, 383.2 > 147.3, 383.2 > 159.0. Deuterated 25-OHC (11099, Sapphire Bioscience, Redfern, Australia) and 7α,25-OHC (700078P, Merck) were used as internal standards. Following MRM transitions were recoded for internal standards 391.1 > 373.2, 391.1 >133.1, 391.1>123.1 (25-OHC) and 407.2 > 389.0 (7α,25-OHC). De-clustering potential (DP), collision energy (CE), entrance (EP) and collision cell exit potential (CXP) were optimised for each MRM pair to maximise the sensitivity. Data was processed using AbSciex

MultiQuant™ software (Version 3.0.3). Oxysterol concentrations were subsequently normalised to the lung weights. High-performance liquid chromatography (HPLC) grade methanol, acetonitrile and chloroform were purchased from Merck.

Flow cytometry

Lung lobes of IAV-infected mice were digested in digestion buffer (Librase; Roche) and passed through 40-µm nylon mesh to obtain single cell suspensions. Red blood cell lysis was performed using BD Pharm Lyse (BD Biosciences, San Jose, CA). Cells were stained with Zombie Green Fixable Viability kit (423111, Biolegend) for 20 mins in PBS first, then stained with fluorescence-conjugated antibodies in FACS buffer for 30 mins on ice before flow cytometric analysis on the BD LSRFortessa X20. The following anti-mouse antibodies were used: Zombie Green Fixable Viability kit (423111, Biolegend), PerCP-CD45 (30-F11), Brilliant Ultraviolet 395-CD3e (145-2C11, BD Biosciences), Brilliant Violet (BV) 786-CD4 (L3T4, BD Biosciences), PE/Cyanine7-CD11b (M1/70), BV510-CD11c (N418), APC/Cyanine7-F4/80 (BM8), BV605-Ly6G (1A8, BD Bioscience), PE-B220 (RA3-6B2), BV421-I-A/I-E (M5/114.15.2), APC-Siglec-F (CD170, S17007L, BD bioscience). Post-acquisition analysis was performed using FlowJo software (TreeStar).

Blood samples were incubated on ice for 40 minutes in mouse CD16/CD32 hybridoma 2.4G2 supernatant to block IgG receptors and fluorescein isothiocyanate (FITC)-conjugated CD11b (M1/70) (101206, Biolegend), anti-CSF1R-PE-Cyanin7 (PECy7) (30-F11) (103149, BD Biosciences), Ly6G-APC-Cyanin7 (APCCy7) (1A8) (127624, BioLegend), and CD45-BV785 (103149, BD Biosciences) antibodies. Fixable viability stain (FVS)700 (564997, BD Bioscience) was added to all stained samples for dead cell exclusion. Samples were analysed on a Cytoflex (Beckman

Coulter) flow cytometer equipped with 640nm, 561nm, 488nm, and 405nm lasers. Uncompensated FCS files were analysed using FlowJo10 software following compensation with single colour controls.

Histology

The left lobe of each mouse (both IAV and SARS-CoV-2) was inflated and fixed in 10% neutral buffered formalin for 24 h before being transferred to 70% ethanol for processing by the Core Histology Facility (Translational Research Institute, Australia). Paraffin-embedded samples were subsequently sectioned, deparaffinized and rehydrated before being stained with hematoxylin and eosin. Histopathological changes were scored by a pathologist blinded to the group treatments as previously described [6, 7].

Immunohistochemistry

Heat-induced epitope retrieval was performed using citrate buffer (pH 6, 95˚C, 30 mins) (BP327-1; Thermo Fisher Scientific). Sections were blocked for endogenous peroxidase activity using 3% hydrogen peroxide (HL001-2.5L-P, Chem Supply, Adelaide, South Australia), washed with tris-buffered saline (TBS; Bio-Rad) containing 0.05% polysorbate 20 (Tween-20; Sigma Aldrich; TBST) and blocked using background sniper (BS966, Biocare Medical, Concord, CA) for 30 mins. Immunolabelling was performed with rabbit antibodies against SARS-CoV-2 nucleocapsid protein antibody (1 hour at 25˚C, 1:5000) (40143-R040 Sino Biological), IBA1 (2 hours at 25˚C 1:1000) (019-19741; NovaChem), CH25H (4˚C overnight 1:600) (BS-6480R, Bioss Antibodies), CYP7B1 (4˚C overnight 1:1000) (BS-5052R, Bioss Antibodies), HSD3B7 (2 hours at 25˚C 1:600) (BS-2366R, Bioss Antibodies) and isotype control (rabbit IgG 31235, Thermo Fisher Scientific. Sections were washed with TBST and subsequently incubated with horseradish peroxidase (HRP)-conjugated goat anti-rabbit Ig antibody (1:200) (ab6721, Abcam) at 25˚C for 30 mins. Sections were washed with TBST before applying chromogen detection, using diaminobenzidine (ab64238, DAB substrate kit Abcam,) as per the manufacturer's instructions. Counterstaining was performed with Mayer’s hematoxylin (Sigma-Aldrich) before dehydrating the sections in a series of increasing ethanol concentrations (70% to 100% ethanol). Sections were clarified with xylene and mounted using a xylene-based mounting medium (15-184-40, SHURMount Mounting Media, Fisher scientific). Slides were scanned in an Olympus SLIDEVIEW VS200 using a 20x objective. DAB-positive areas were quantified using ImageJ (https://imagej.nih.gov/ij/) using a method previously described [8].

Mouse tissue sampling

At the endpoint of the experiments, mice were euthanised with CO2. The BM of one femur was flushed into 1 mL ice-cold phosphate buffered saline (PBS) containing 2% newborn calf serum (NCS) using a 1 mL syringe mounted with a 23G needle, and cells washed in this buffer for subsequent flow cytometry and colony assays. Blood was collected via cardiac puncture using a 1 mL syringe mounted with a 26G needle. Blood samples for flow cytometry were first cleaned by erythrocyte lysis by a 5-minute incubation in 5 volumes of 10 mM NaHCO3, 150 mM NH4Cl, 1 mM EDTA pH=7.4 buffer at room temperature. Blood leukocytes were then washed twice by centrifugation in PBS with 2% NCS. Blood samples were counted neat on Mindray BC-5000 Vet Auto hematology analyzer (Biomedical Electronics Co. LTD., China).

Bone marrow derived macrophage (BMDM) preparation and cell viability

BMDM were prepared by flushing the BM of 1 femur with PBS containing 2 % NCS. BM cells were washed with PBS and then diluted in 200µl RPMI-1640 supplemented with 10% fetal calf serum (FCS, Life Technologies), 100ng/mL recombinant human macrophage colony-stimulating factor-1 (CSF1 was a kind gift from Prof David Hume, Mater Research), standard penicillin, gentamycin and glutamine and seeded in six 10 cm diameter Sterilin™ dishes (ThermoFisher Scientific, cat#SLN109) and 50,000 cells/well were cultured at 37ºC with 5% CO_2.

Colony forming assay

Bone marrow cell suspension aliquots corresponding to 1/1000 of a whole femoral marrow (in 10µL) were seeded in duplicate in 35 mm Petri dishes and covered with 1mL cytokine-free MethoCult medium (Cat# M3231, Stem Cell Technologies, Vancouver, Canada) supplemented with 100-ng/mL recombinant human CSF-1 (kindly donated by Prof David Hume). Colony forming units macrophage (CFU-M) were counted after 8 days of culture at 37 ºC in a 5% CO_2 humidified incubator.

In vitro infection/stimulation with IAV and LPS

Bone marrow cells from the femur and tibia of 3 C57BL/6 and 3 *Gpr183-/-* mice were extracted as previously described [9]. 10 x 10^6 bone marrow cells were cultured in 10 ml of complete media (DMEM, 100 U/ml of penicillin-streptomycin and 10% FBS) in the presence of recombinant mouse macrophage colony-stimulating factor (mouse CSF-1; 50 ng/ml; Peprotech). On day 3, 10 ml of complete media containing 50 ng/ml CSF-1 was added. On day 6, adherent cells were collected as BMDMs. BMDMs were re-seeded to 24 well plates at a density of $3x10^5$ cell/ml, left overnight in incubator before infection and/or stimulation. BMDMs are subsequently infected with A/Solomon Islands/03/06 at a multiplicity of infection (MOI) of 10, with or without 10µM NIBR189 for one hour. After one hour, cells were washed with DMEM containing 25mM HEPES (Thermofisher, 15630106) to remove excess viruses before media replacement containing NIBR189 for 24 hours. Cells were stimulated with LPS (100ng/mL) with or without 10µM NIBR189 for 24 hours. For RNA extraction, cells were lysed by adding 500 µL of TRIZol reagent.

Analysis of single cell RNA sequencing data

We accessed publicly available single cell RNA sequencing (scRNA-seq) data from nine COVID-19 patients (moderate: *n* = 3; severe: *n* = 6) and four healthy controls [10]. The dataset comprised a total of 66,452 cells from 32 cell type clusters, including eight major BALF immune cell types (i.e., macrophages, neutrophil, myeloid dendritic cells [mDCs], plasmacytoid dendritic cells [pDCs], T, NK, B, plasma), epithelial cells, and mast cells. We then tested for evidence of differential expression of four genes (*CH25H*, *CYP7B1*, *GPR183, HSD3B7*) between: (1) moderate COVID-19 cases and healthy controls; (2) severe COVID-19 cases and healthy controls; (3) COVID-19 cases and healthy controls; and (4) severe and moderate COVID-19 cases, for each major BALF cell type cluster and 16 macrophage sub-clusters. We estimated the average log fold change (logFC) per gene between groups using negative binomial generalised linear models applied to the raw unique molecular identifier (UMI) counts implemented in the Seurat software [11], and adjusted for covariates, including number of total UMI count per cell, number of genes detected per cell, and percent mitochondrial genes per cell. We also applied a non-parametric Wilcoxon rank sum test for normalised counts as a sensitivity analysis. We used Bonferroni correction to identify significant associations ($p < 1.30\times10^{-4}$; i.e., $\frac{0.05}{24\ clusters \times 4\ genes \times 4\ comparisons}$) and further required that genes be expressed in at least 5% of cells in both groups with an absolute value of average log fold change (logFC) greater than 0.25.

Supplementary figures

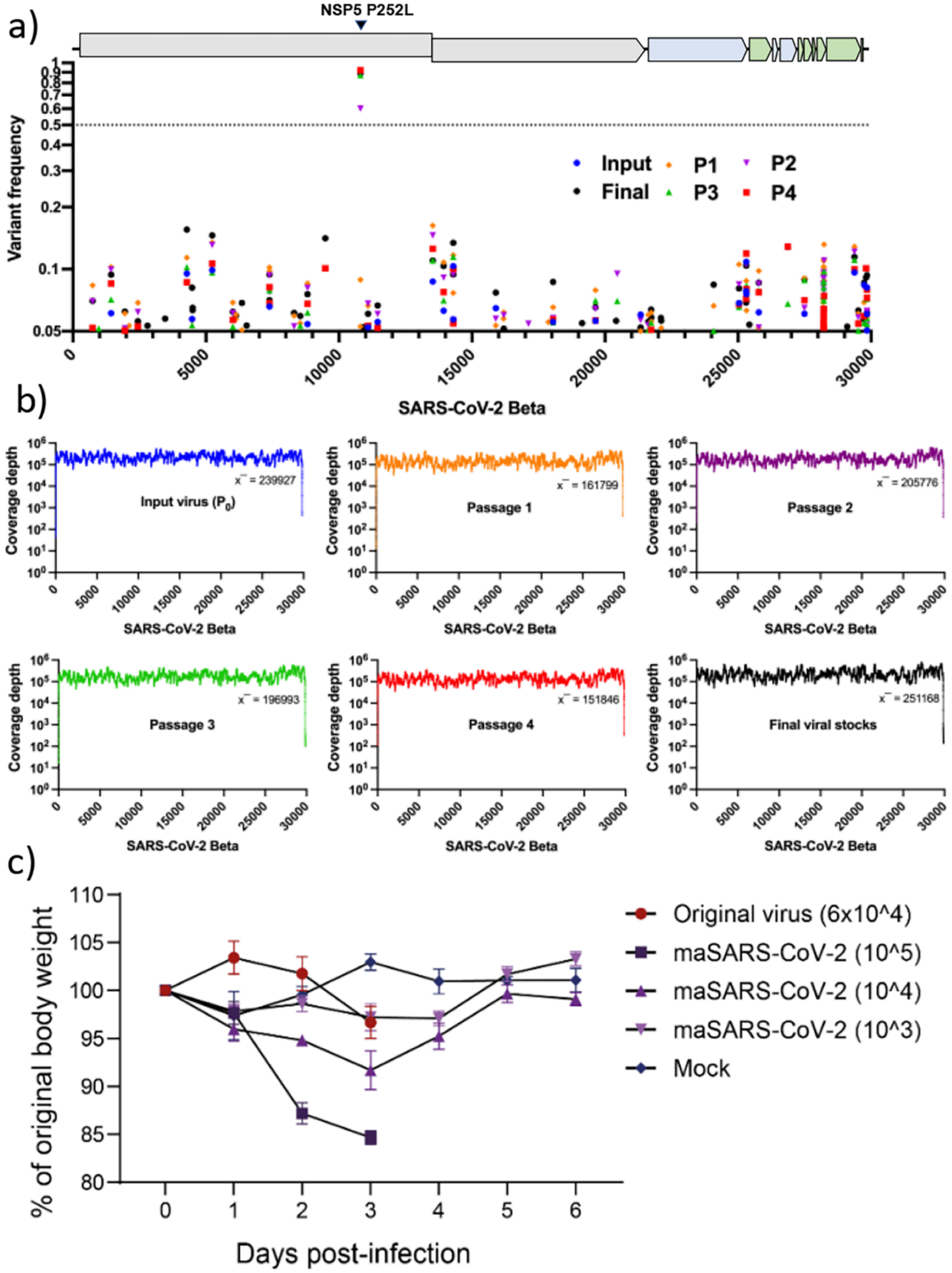

Figure S1. Evolution and coverage of mouse-adapted SARS-CoV-2 virus. a) Mutation frequency of input SARS-CoV-2 Beta virus (blue circle) and passage one (orange diamond), passage two (purple nabla), passage three (green triangle) and passage four (red square) mouse-adapted viruses over the reference genome sequence as well as the final virus stocks (black circle) amplified in VeroE6-hTMPRSS2 cells. The dotted line indicates the consensus frequency of 0.5 b) Summary plots of read coverage of passaged SARS-CoV-2 viruses from a) mapping to SARS-CoV-2 Beta strain. Depth of coverage of binary alignment files was determined using samtools depth. c) Weight loss over time following infection with the Beta variant of SARS-CoV-2 (original virus) or various doses of maSARS-CoV-2 (after four passages in mice). Plaque forming units are indicated in brackets. Data indicates mean ± SEM.

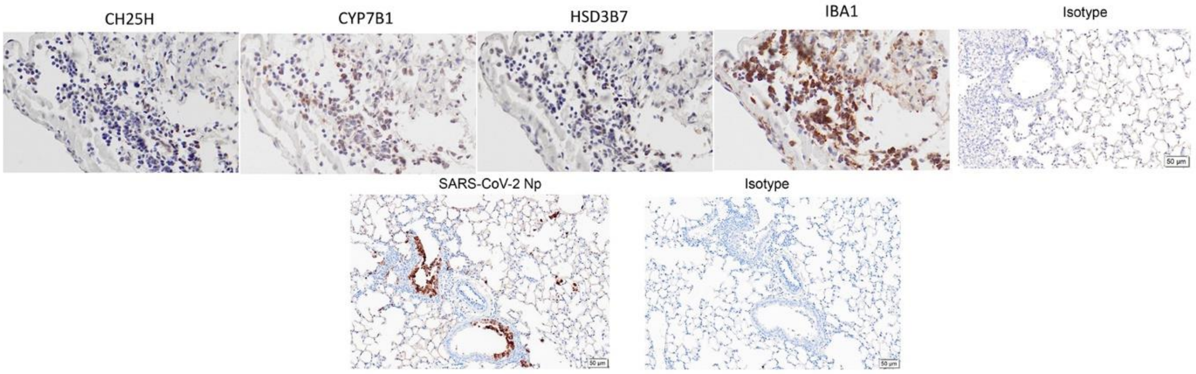

Figure S2. Isotype staining controls for CYP7B1, CH25H, IBA1 and viral Np. IHC of IAV-infected lung sections incubated with rabbit anti-CH25H, rabbit anti-CYP7B, rabbit anti-HSD3B7, rabbit anti-IBA1 and an isotype-matched control (Rabbit IgG; negative control). IHC of SARS-CoV-2-infected lung sections incubated with rabbit anti-SARS-CoV-2 nucleocapsid protein (Np) and an isotype-matched control (Rabbit IgG; negative control). Scale bar = 50μm

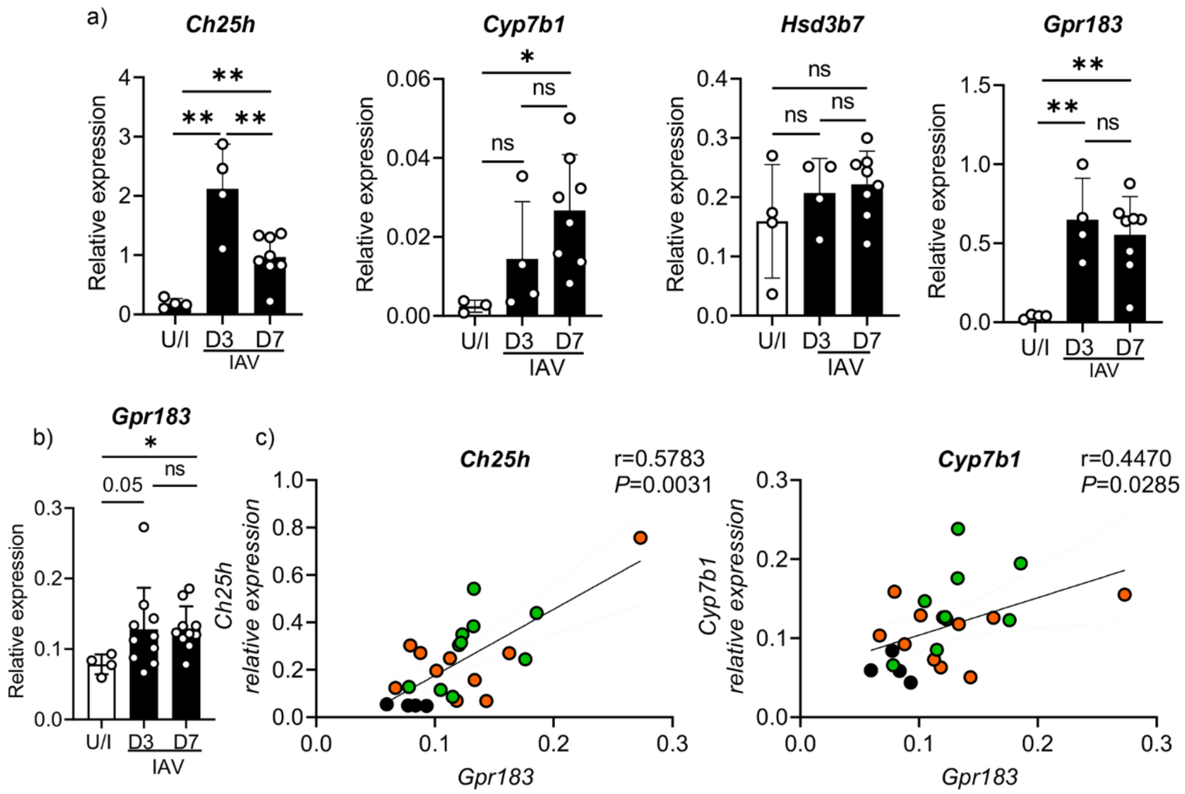

Figure S3. *Ch25h, Cyp7b1, Hsd3b7* and *Gpr183* mRNA expression is upregulated in the BAL cells during IAV infection and *Gpr183* expression in the lung tissue correlates with expression of the oxysterol synthesising enzymes CH25H and CYP7B1. C57BL/6J mice were infected intranasally with 5,500 PFU of IAV. Relative expression of *Ch25h*, *Cyp7b1*, *Hsd3b7* and *Gpr183* mRNA measured by RT-qPCR, normalised to *Hprt from a) BAL cell pellet and b) lung tissue*. Correlation analyses were performed with mRNA expression levels of *Gpr183* and oxysterol synthesising enzymes from lung tissue. Individual scatter plots showing correlations between *Gpr183* and *Ch25h* and *Cyp7b1*. Black dots represent uninfected samples while coloured dots represent IAV-infected samples (Orange dots, 3 dpi; green dots, 7 dpi). Data are presented as mean ± SD of n=4 uninfected and n=8-10 infected mice per timepoint. ns = not significant; *, $P < 0.05$; **, $P < 0.01$ indicate significant differences. Spearman rank correlation test were used to calculate the correlation coefficient and to determine significant correlations with values displayed on each scatter plot.

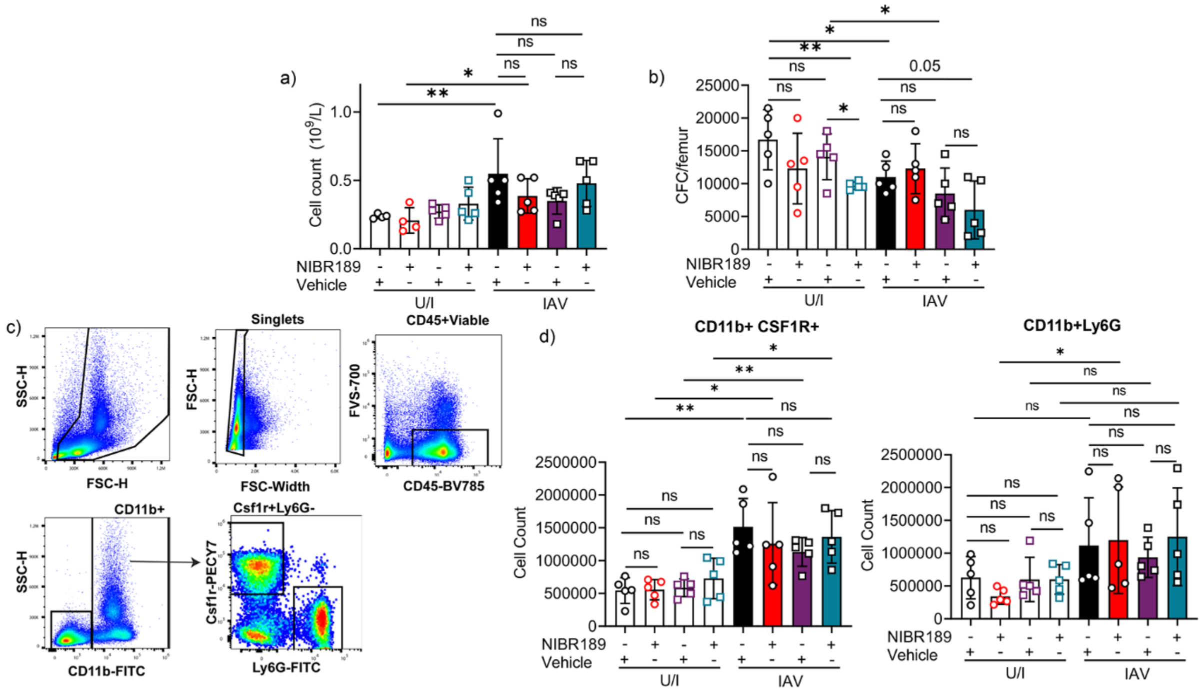

Figure S4. C57BL/6J or *Gpr183*$^{-/-}$ mice were infected intranasally with 5,500 PFU of IAV or mock infected (U/I). Mice were subsequently treated orally with 7.6 mg/kg NIBR189 or vehicle control twice daily from 1 dpi until the end of the experiment. a) blood monocyte cell counts on differential blood analyser b) bone marrow CFU-M numbers per femur in colony forming assays with recombinant CSF-1, c) gating strategy and d) cell counts (cells per mL blood) of CD45$^+$ CD11b$^+$ CSF1R$^+$ Ly6G$^-$ monocytes and CD45$^+$ CD11b$^+$ CSF1R$^-$ Ly6G$^+$ neutrophils by flow cytometry.

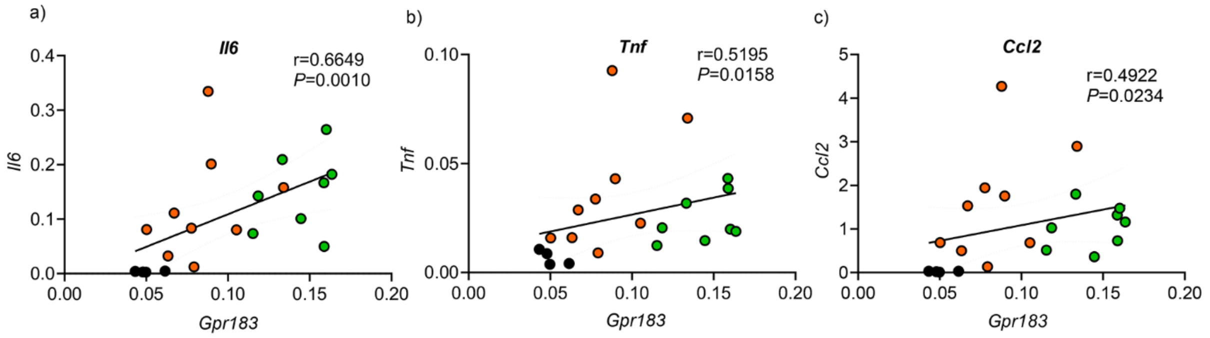

Figure S5. **Correlations between lung mRNA expression of *Gpr183* and inflammatory markers in IAV-infected mice.**

Correlation analyses of *Gpr183* mRNA expression with mRNA expression of inflammatory cytokines in lung tissue from IAV-infected C57BL/6J mice (n=21 pairs). Relative gene expression was determined by RT-qPCR, normalised to *Hprt*. Individual scatter plots showing correlations between *Gpr183* and a) *Il6*, b) *Tnf* and c) *Ccl2*. Black dots represent uninfected samples while coloured dots represent IAV-infected samples (orange dots, 3dpi; green dots, 7dpi). Spearman rank correlation tests were used to calculate correlation coefficient and to determine significant correlations with values displayed on each scatter plot.

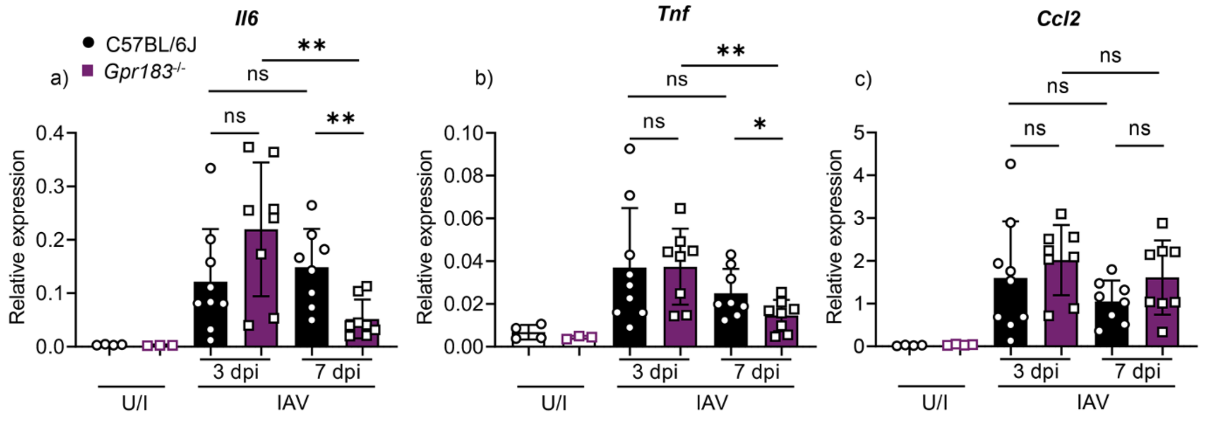

Figure S6. Cytokine expression at mRNA and protein level in IAV-infected C57BL/6J and *Gpr183*$^{-/-}$ mice. C57BL/6J and *Gpr183*$^{-/-}$ mice were infected intranasally with 5,500 PFU of IAV. Cytokine measurements of a) *Il6,* b) *Tnf* and c) *Ccl2* at 3 dpi and 7 dpi measured by RT-qPCR, normalised to *Hprt.* Data are presented as mean ± SD of n=4 uninfected per genotype and n=8-10 infected mice per genotype and timepoint. U/I = uninfected; dpi = days post-infection; ns = not significant; *, $P < 0.05$; **, $P < 0.01$ indicate significant differences.

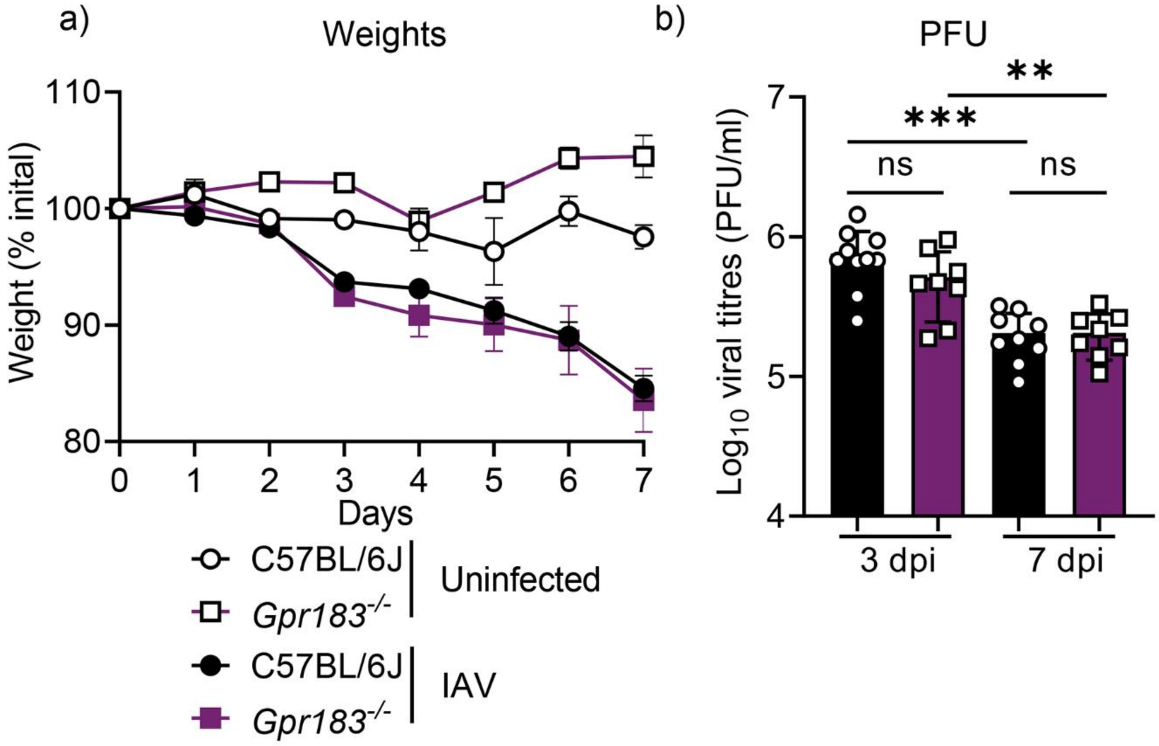

Figure S7. Weights of IAV and mock infected C57BL/6J and *Gpr183*$^{-/-}$ mice and viral loads. C57BL/6J and *Gpr183*$^{-/-}$ mice were infected intranasally with approximately 5,500 PFU of IAV. a) Weights of IAV- or uninfected, mock-inoculated mice are displayed as percentage of the weight at time of inoculation. b) Viral loads were assessed by measuring the PFU by plaque assays. Data are presented as mean ± SD for n=8-10 infected mice per genotype and timepoint. dpi = days post-infection; ns = not significant; **, *P* < 0.01; ***, *P* < 0.001 indicate significant differences.

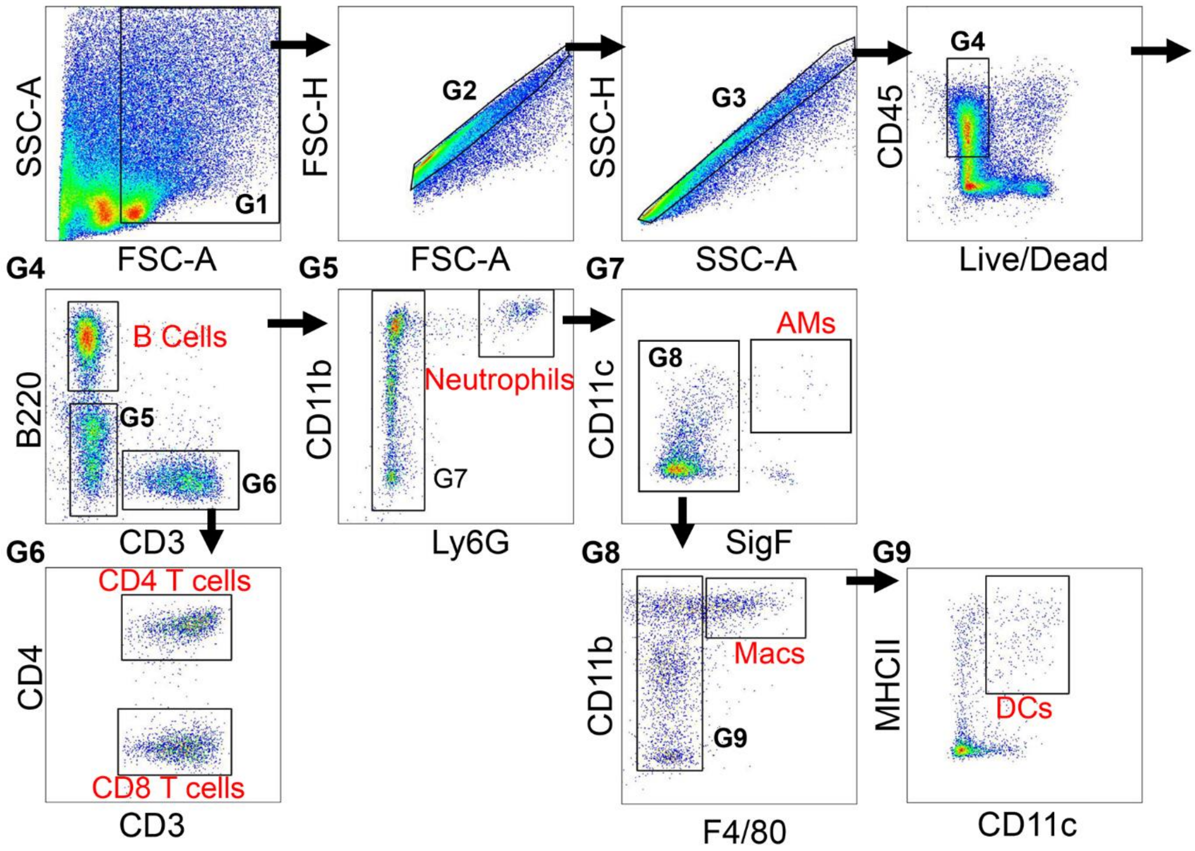

Figure S8. Representative flow cytometry plots illustrating the gating strategy for immune cells in lung single cells suspension. Gates containing multiple cell populations are numbered (G1-G9). Gates that contained a single cell population are labeled with its respective cell type. These includes: B cells (B220$^+$; G5), CD4$^+$ T cells (CD3$^+$,CD4$^+$; G6), CD8$^+$ T Cells (CD3$^+$,CD4$^-$; G6), Neutrophils (B220$^-$,CD3$^-$,Ly6G$^+$; G5), Alveolar macrophages (B220$^-$,CD3$^-$,Ly6G$^-$,CD11c$^+$,SigF$^+$; G7), Macrophages (B220$^-$,CD3$^-$,Ly6G$^-$,SigF$^-$,CD11b$^+$,F4/80^{high}; G8) and Dendritic cells (DCs; B220$^-$,CD3$^-$,Ly6G$^-$,SigF$^-$, F4/80^{low},CD11c$^+$, MHCII$^+$; G9).

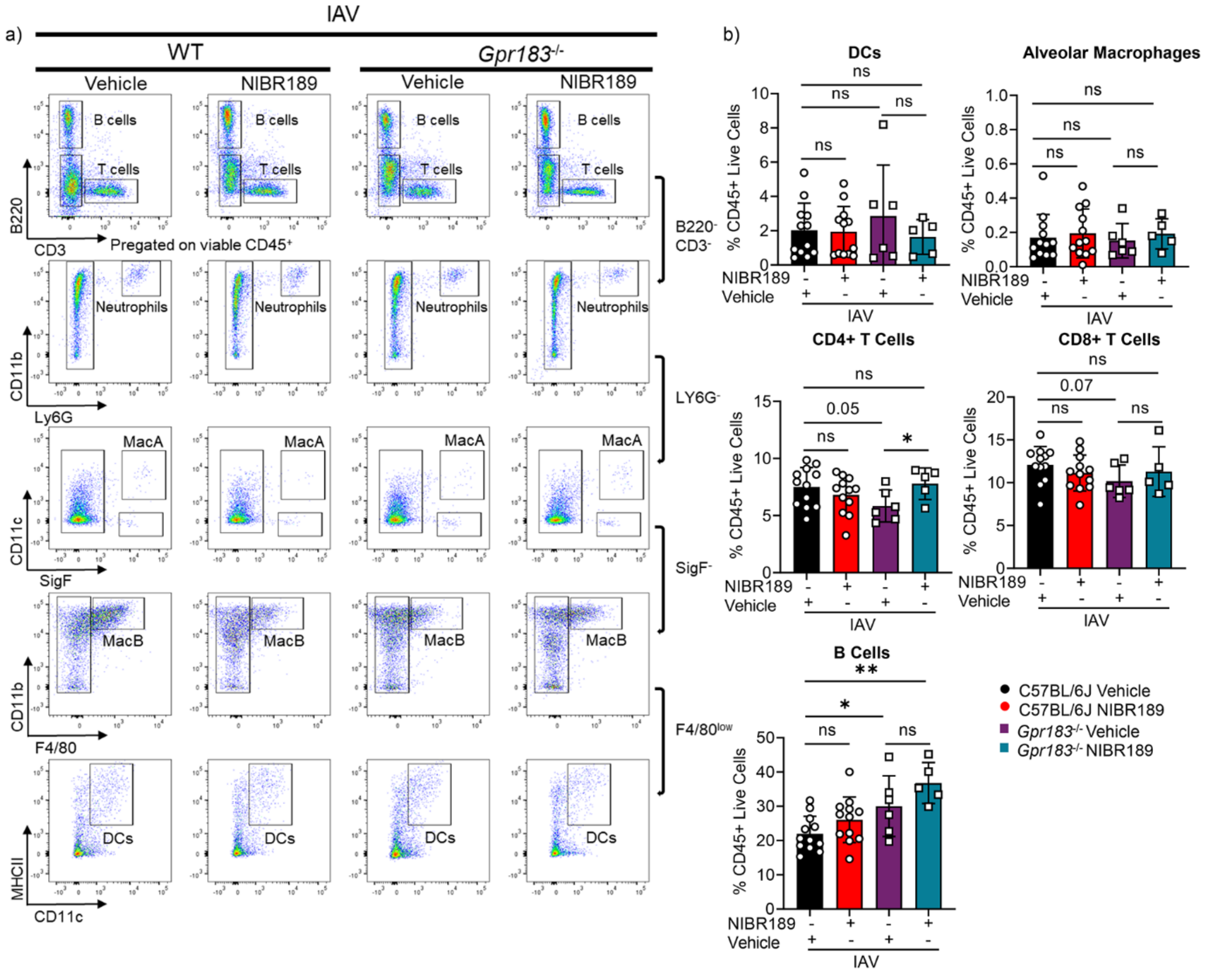

Figure S9. Immune cell populations in the lungs of IAV-infected mice treated with the GPR183 antagonist NIBR189. C57BL/6J or *Gpr183*$^{-/-}$ mice were infected intranasally with 5,500 PFU of IAV. Mice were subsequently treated orally with 7.6 mg/kg NIBR189 or vehicle control twice daily from 1 dpi until the end of the experiment. a) Frequencies of B cells (B220^{+}), T cells (CD3^{+} CD8^{+} or CD4^{+}), neutrophils (B220^{-}CD3^{-}Ly6G^{+}) were determined by flow cytometry against total viable CD45^{+} immune cells at 3 dpi. Alveolar macrophages (CD11c^{+}SigF^{+}), infiltrating macrophages (F480^{high}/CD11b^{+}/Ly6G^{-}/SigF^{-}) and dendritic cells (SigF^{-}F4/80^{-} MHCII^{+}CD11c^{+}) were further identified from the B220^{-}CD3^{-}Ly6G^{-} cell population. B) Graphs depicting the frequency of Dendritic cells, alveolar macrophages, CD4^{+} T cells, CD8^{+} T cells and B cells against total viable CD45^{+} immune cells. Data are presented mean ± SD of n=5-12 infected mice per genotype and timepoint. UI = uninfected; dpi = days post-infection; ns = not significant.

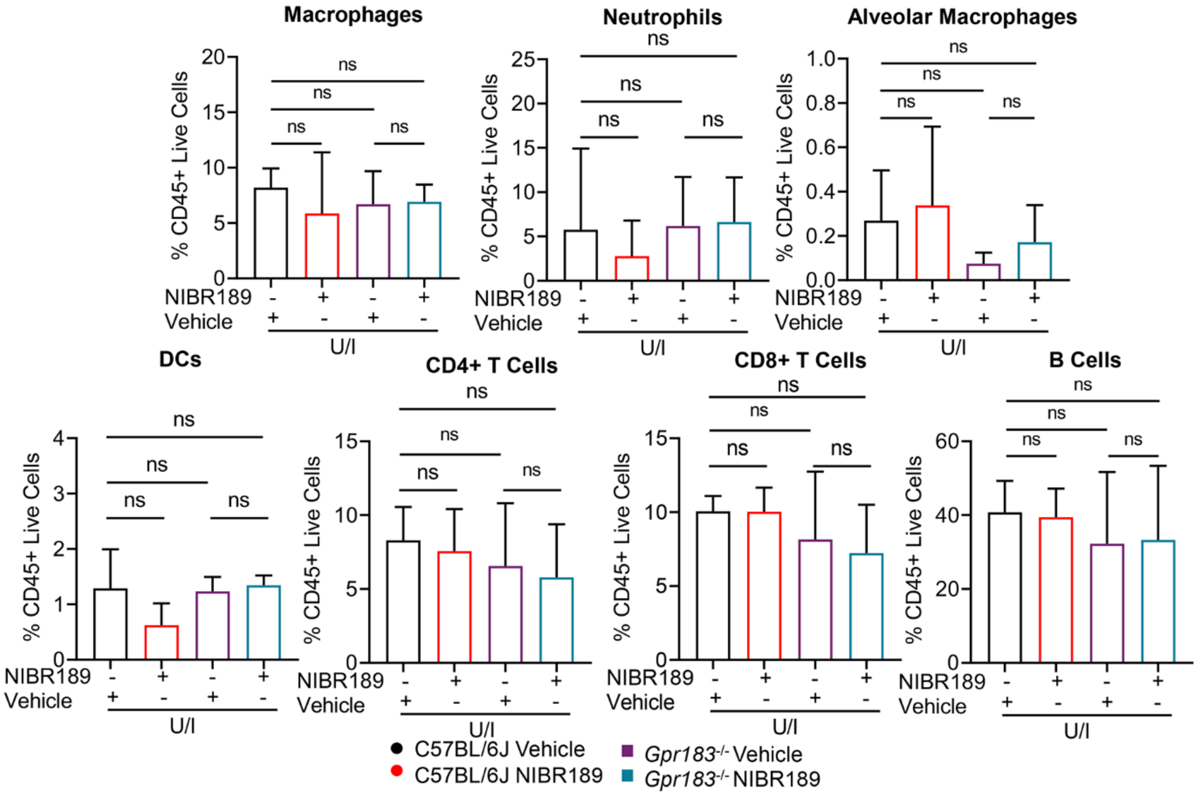

Figure S10. Immune cell populations in the lungs of uninfected mice treated with the GPR183 antagonist NIBR189. C57BL/6J or *Gpr183*$^{-/-}$ mice were mock infected intranasally with PBS. Mice were subsequently treated orally with 7.6 mg/kg NIBR189 or vehicle control twice daily from 1 dpi until the end of the experiment. Graphs show the frequencies of macrophages, neutrophils, alveolar macrophages, B cells CD4^{+} T cells, CD8^{+} T cells and Dendritic cells against total viable CD45^{+} immune cells at 3 dpi. Data are presented mean ± SD of n=2-3 uninfected mice per genotype and timepoint. UI = uninfected; ns = not significant.

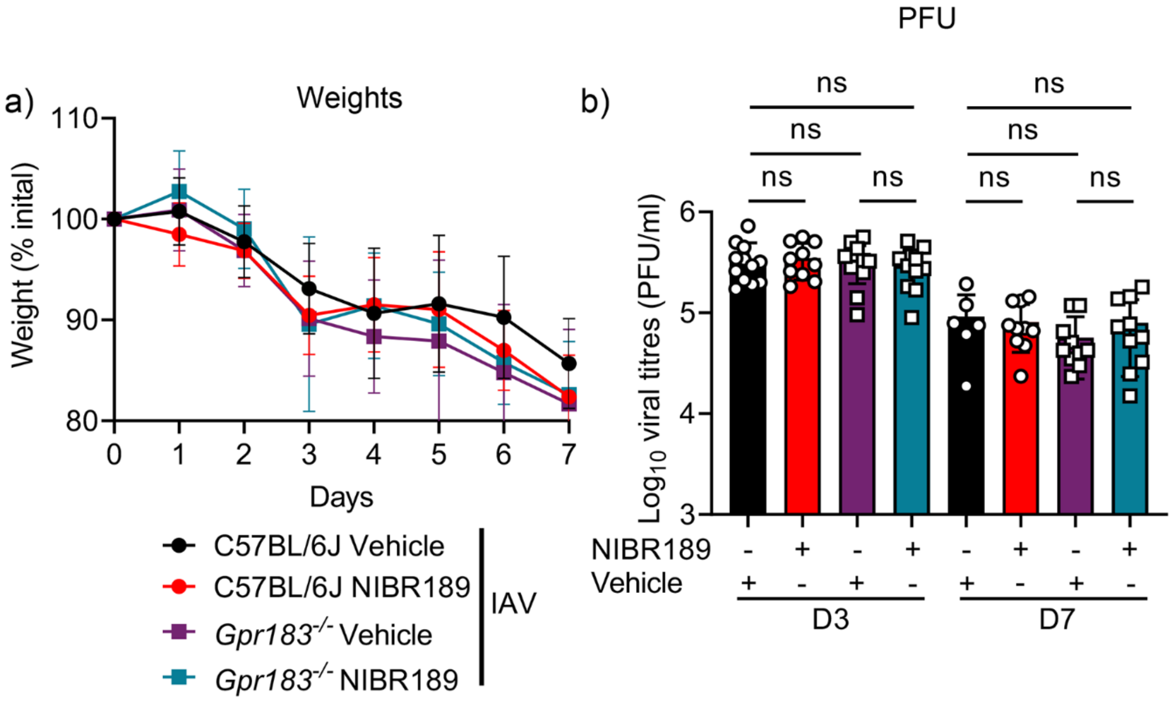

Figure S11. Body weights and viral loads of IAV-infected C57BL/6J and *Gpr183*$^{-/-}$ mice treated with NIBR189 or vehicle. C57BL/6J mice and *Gpr183*$^{-/-}$ mice were infected intranasally with 5,500 PFU of IAV. Mice were subsequently treated orally with 7.6 mg/kg NIBR189 or vehicle control twice daily from 1 dpi until the end of the experiment. a) Weights of IAV- or mock-inoculated mice with or without treatment are displayed as percentage of the weight at time of inoculation. b) Viral loads were assessed by measuring the PFU by plaque assay. Data are presented as mean ± SEM or SD of n=6-12 infected mice per genotype and timepoint. UI = uninfected; dpi = days post-infection; ns = not significant.

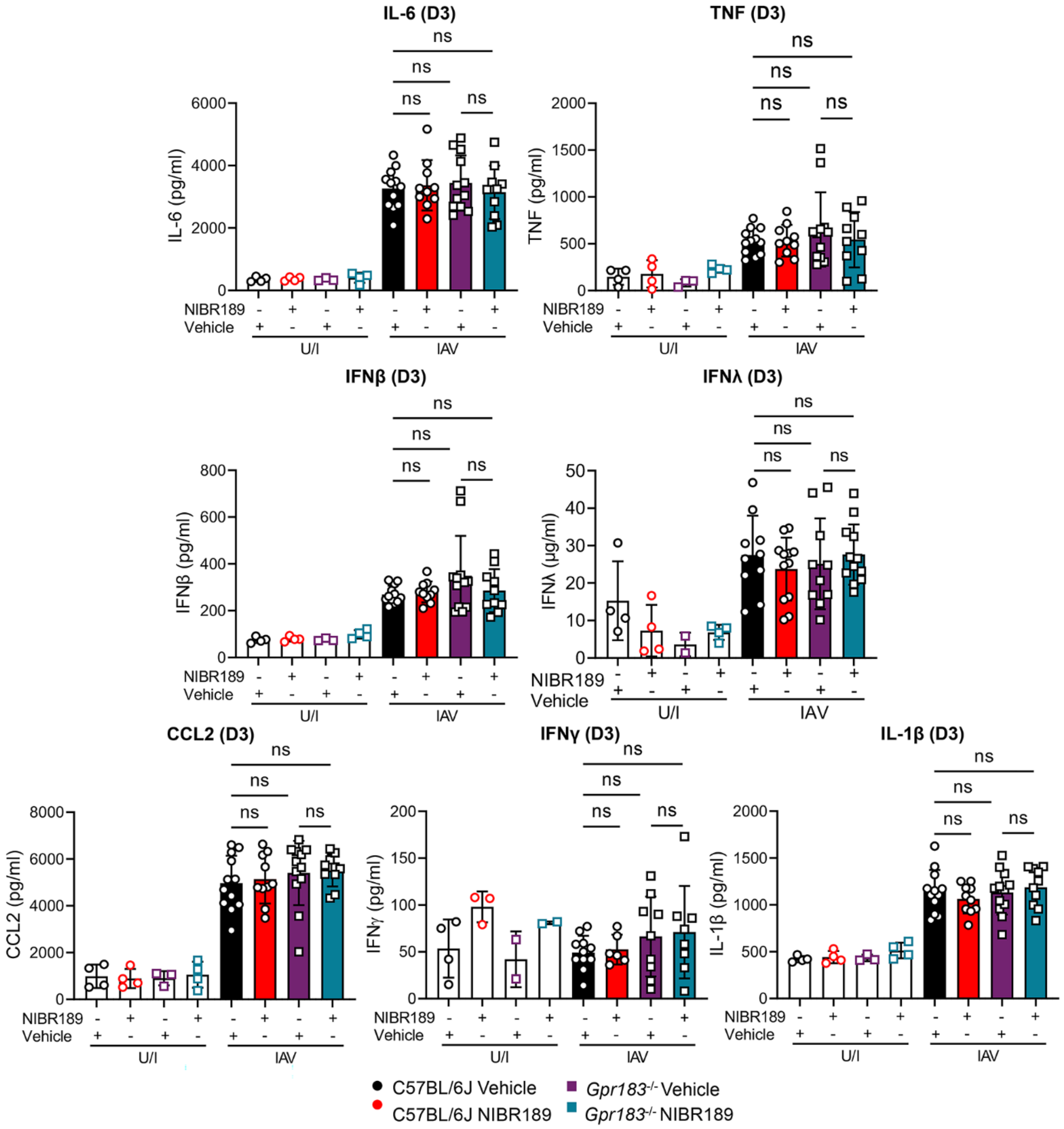

Figure S12. Cytokine concentrations in IAV-infected C57BL/6J and *Gpr183*$^{-/-}$ mice treated with NIBR189 and/or vehicle. C57BL/6J and *Gpr183*$^{-/-}$ mice were infected intranasally with 5,500 PFU of IAV. Mice were subsequently treated orally with 7.6 mg/kg NIBR189 or vehicle control twice daily from 1 dpi until the end of the experiment. Cytokine measurements of IL-6 TNF, IFNβ, IFN*λ*, CCL2 IFNγ and IL-1β, at 3 dpi measured by ELISA. Data are presented as mean ± SD of n=4 uninfected mice per genotype and n=6-12 infected mice per genotype. U/I = uninfected; dpi = days post-infection; ns = not significant. *, $P < 0.05$ indicate significant differences.

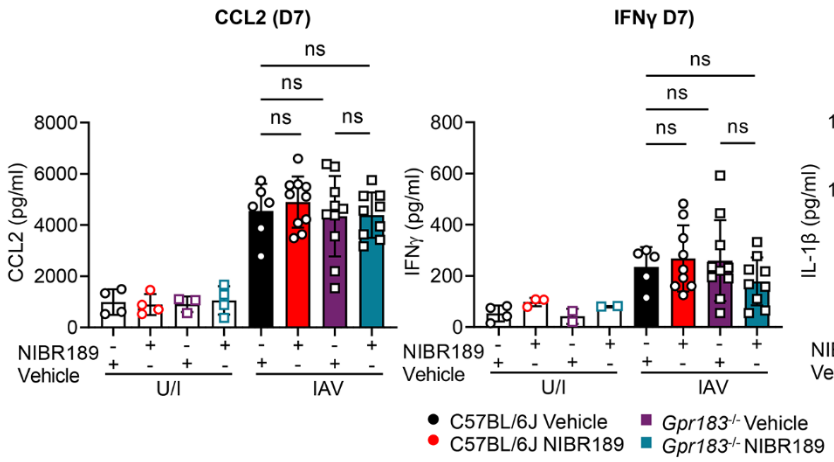

Figure S13. Cytokine concentrations in IAV-infected C57BL/6J and *Gpr183*$^{-/-}$ mice treated with NIBR189 and/or vehicle. C57BL/6J and *Gpr183*$^{-/-}$ mice were infected intranasally with 5,500 PFU of IAV. Mice were subsequently treated orally with 7.6 mg/kg NIBR189 or vehicle control twice daily from 1 dpi until the end of the experiment. Cytokine concentrations of CCL2, IFNγ, and IL-1β at 7 dpi were measured by ELISA. Data are presented as mean ± SD of n=4 uninfected mice per genotype and n=6-12 infected mice per genotype. U/I = uninfected; dpi = days post-infection; ns = not significant.

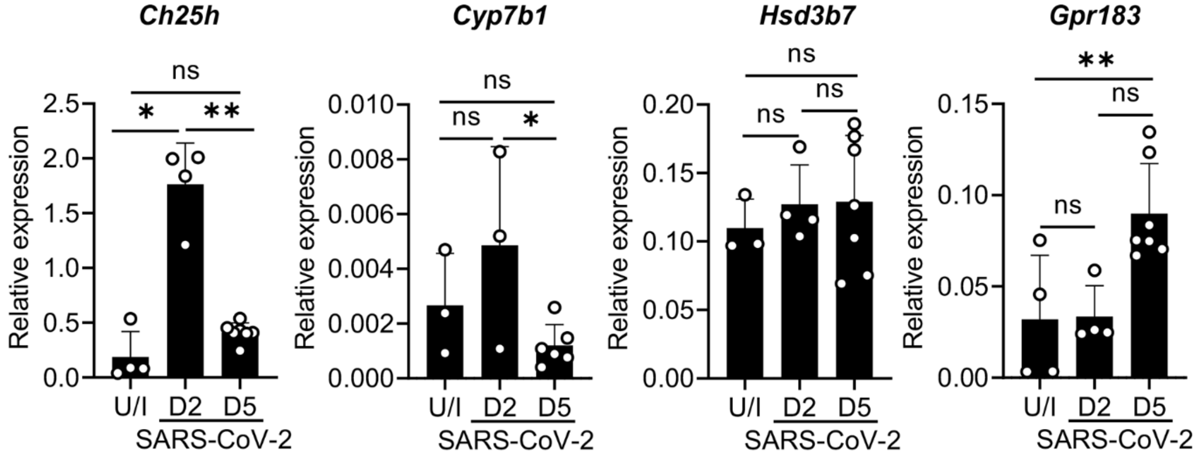

Figure S14. *Gpr183, Ch25h, Cyp7b1* and *Hsd3b7* mRNA expression in BALF during SARS-CoV-2 infection. C57BL/6J and *Gpr183*$^{-/-}$ mice were infected intranasally with approximately 8x10^{4} PFU of mouse-adapted SARS-CoV-2. Relative expression of *Gpr183*, *Ch25h*, *Cyp7b1*, *Hsd3b7* and *Gpr183* mRNA measured by RT-qPCR, normalised to *Hprt in BAL cells*. Data are presented as mean ± SD of n=3-4 uninfected and n=4-7 infected mice per timepoint. ns = not significant; *, $P < 0.05$; **, $P < 0.01$ indicate significant differences.

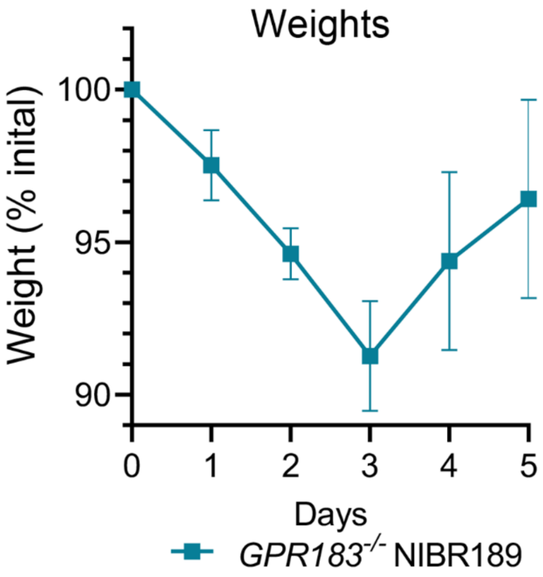

Figure S15. Body weights of *Gpr183-/-* mice upon SARS-CoV-2 infection. *Gpr183*$^{-/-}$ mice were infected intranasally with approximately 8x10^{4} PFU of mouse-adapted SARS-CoV-2. Mice were subsequently treated orally with 7.6 mg/kg NIBR189 or vehicle control twice daily from 1 dpi until the end of the experiment. Weights of mice displayed as percentage of the weight at time of inoculation. Data are presented as mean ± SEM, n=10.

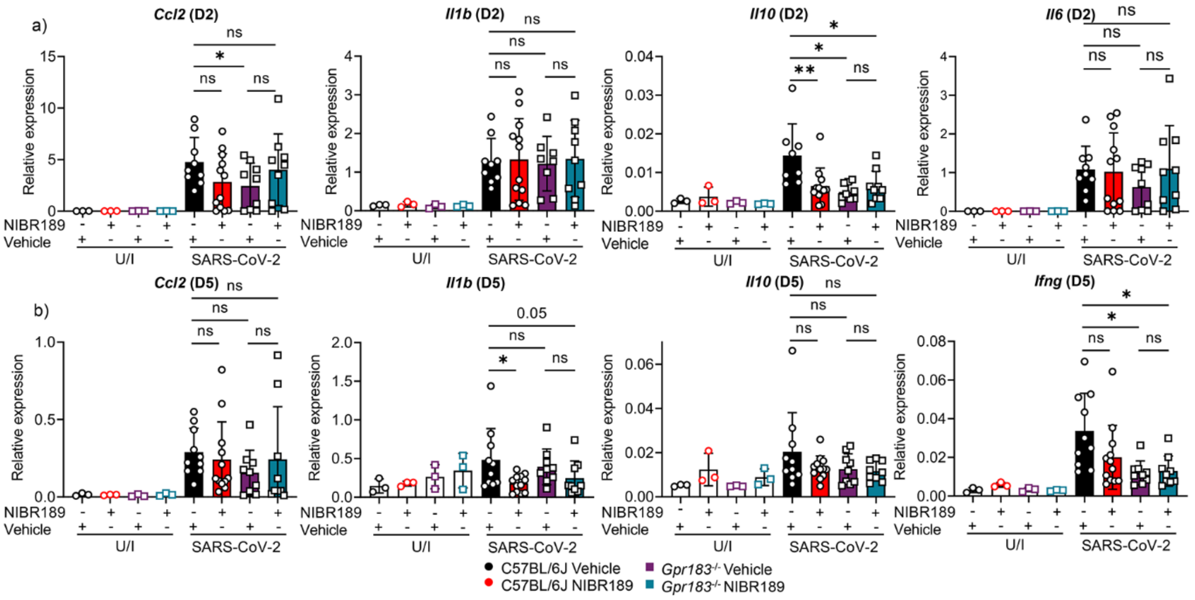

Figure S16. Cytokine mRNA expression in SARS-CoV-2-infected C57BL/6J and *Gpr183$^{-/-}$* mice treated with GPR183 antagonist at 2 dpi and 5 dpi. C57BL/6J and *Gpr183$^{-/-}$* mice were infected intranasally with approximately 8x10^4 PFU of mouse-adapted SARS-CoV-2. Mice were subsequently treated orally with 7.6 mg/kg NIBR189 or vehicle control twice daily from 1 dpi until the end of the experiment. Expression of a) *Ccl2*, *Il1b Il10* and *Il6* at 2 dpi and b) *Ccl2*, *Il1b, Il10* and *Ifng* 5 dpi was measured by RT-qPCR normalised to *Hprt*. Data are presented as mean ± SD of n=3 uninfected mice and n= 9-12 infected; mice per genotype and timepoint. U/I = uninfected dpi = days post-infection; ns = not significant. *, $P < 0.05$; **, $P < 0.01$; ***, $P < 0.001$ indicate significant differences.

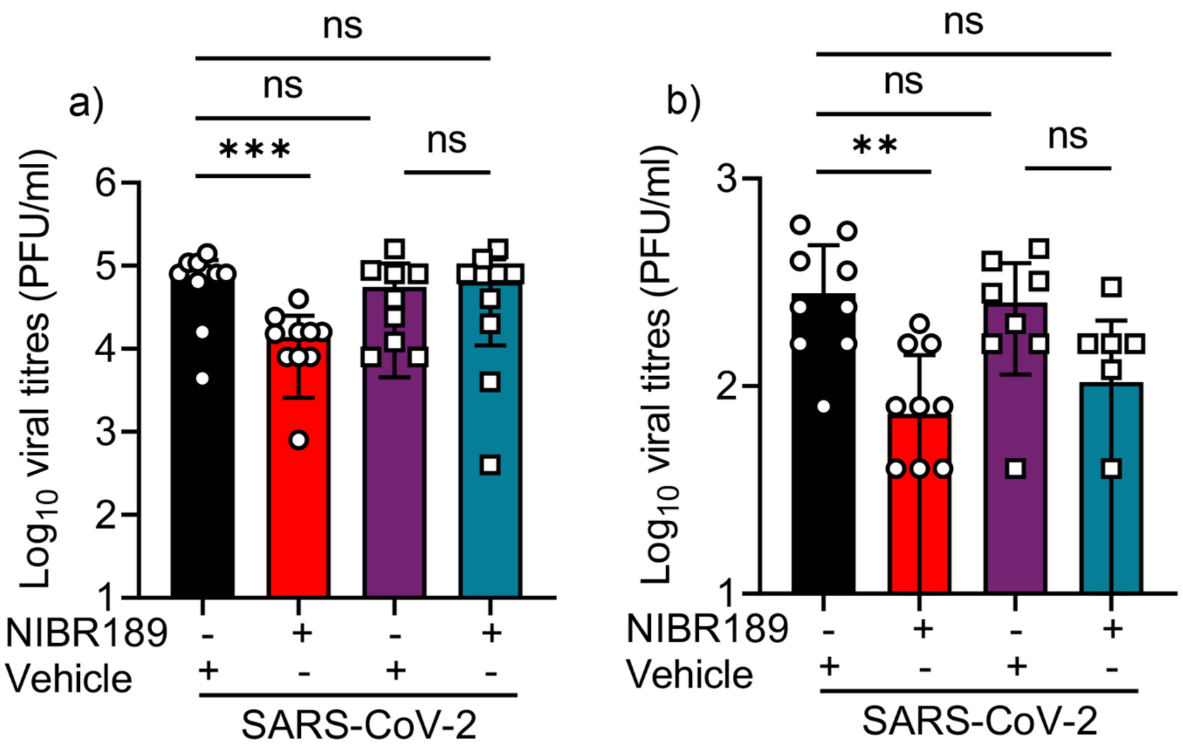

Figure S17. Viral loads of SARS-CoV-2-infected C57BL/6J and *Gpr183*$^{-/-}$ mice treated with NIBR189 or vehicle. C57BL/6J and *Gpr183*$^{-/-}$ mice were infected intranasally with approximately 8x10^{4} PFU of mouse-adapted SARS-CoV-2. Mice were subsequently treated orally with 7.6 mg/kg NIBR189 or vehicle control twice daily from 1 dpi until the end of the experiment. Viral loads were assessed by measuring the PFU through plaque assay. Data are presented as mean ± SEM or SD of n=6-12 infected mice per genotype and timepoint. UI = uninfected; dpi = days post-infection; ns = not significant. ns = not significant. *, $P < 0.05$; **, $P < 0.01$; ***, $P < 0.001$ indicate significant differences.

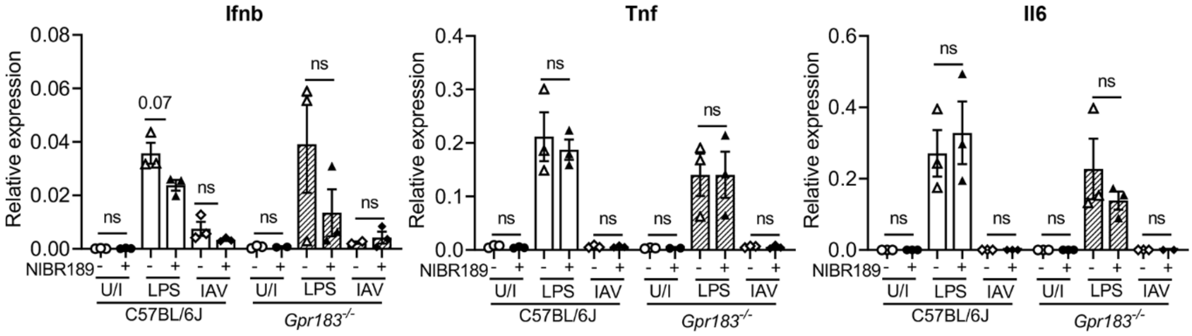

Figure S18. Cytokine mRNA expression in IAV-infected BMDMs from C57BL/6J and *Gpr183*$^{-/-}$ mice treated with GPR183 antagonist. BMDMs were infected with A/Solomon Islands/03/06 at a multiplicity of infection (MOI) of 10, with or without 10µM NIBR189 for one hour. After one hour, cells were washed to remove excess viruses before media replacement containing NIBR189 for 24 hours. Cells were stimulated with LPS (100 ng/mL) with or without 10µM NIBR189 for 24 hours, thereafter mRNA expression of *tnf*, *il6* or *ifnb* was determined by RT-qPCR normalised to *Hprt.*

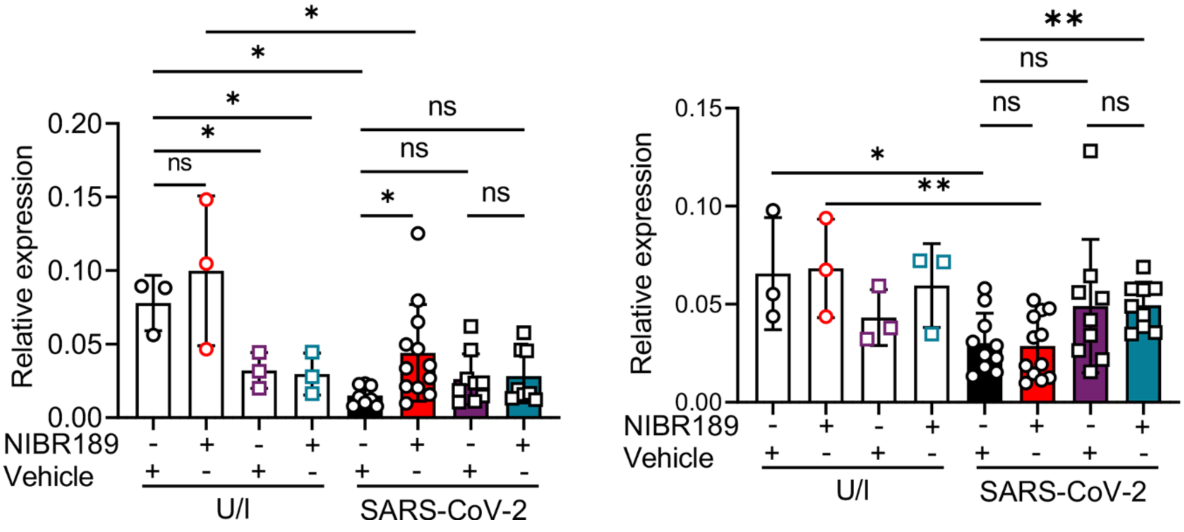

Figure S19. *Ace2* mRNA expression in the lung during SARS-CoV-2 infection. C57BL/6J and *Gpr183*$^{-/-}$ mice were infected intranasally with approximately 8x10^4 PFU of mouse-adapted SARS-CoV-2. Relative expression of *Ace2* mRNA was measured by RT-qPCR, normalised to *Hprt* in lung tissue. Data are presented as mean ± SD of n=3-4 uninfected and n=4-7 infected mice per timepoint. ns = not significant; *, $P < 0.05$; **, $P < 0.01$ indicate significant differences.

Supplemental Table S1: Primers used in this study

	Forward	**Reverse**
Gpr183	GTCGTGTTCATCCTGTGCTTCAC	TCATCAGGCACACCGTGAAGTG
Ch25h	CTGACCTTCTTCGACGTGCT	GGGAAGTCATAGCCCGAGTG
Cyp7b1	CGGAAATCTTCGATGCTCCAAAG	GCTTGTTCCGAGTCCAAAAGGC
Hsd3b7	ACTGCGCTTTGGAGGTCGTCTA	GCCACCAGTATGTGCATCCAAG
Ccl2	GCTACAAGAGGATCACCAGCAG	GTCTGGACCCATTCCTTCTTGG
Hprt1	CCCCAAAATGGTTAAGGTTGC	AACAAAGTCTGGCCTGTATCC
Ifnb1	AACTCCACCAGCAGACAGTG	GGTACCTTTGCACCCTCCAG
Ifng	CAGCAACAGCAAGGCGAAAAAGG	TTTCCGCTTCCTGAGGCTGGAT
Il10	CGGGAAGACAATAACTGCACCC	CGGTTAGCAGTATGTTGTCCAGC
Il1b	TGGACCTTCCAGGATGAGGACA	GTTCATCTCGGAGCCTGTAGTG
Il6	CTGCAAGTGCATCATCGTTGTTC	TACCACTTCACAAGTCGGAGGC
Ifnl	AGCTGCAGGCCTTCAAAAAG	TGGGAGTGAATGTGGCTCAG
Tnf	TAGCCCACGTCGTAGCAAAC	ACAAGGTACAACCCATCGGC
mpro	GAGACAGGTGGTTTCTCAATCG	ACGGCAATTCCAGTTTGAGC
Ace2	TCCATTGGTCTTCTGCCATCC	AACGATCTCCCGCTTCATCTC

References

1. Langmead B, Salzberg SL. Fast gapped-read alignment with Bowtie 2. Nat Methods 2012: 9(4): 357-359.

2. Grubaugh ND, Ladner JT, Lemey P, et al. Tracking virus outbreaks in the twenty-first century. Nat Microbiol 2019: 4(1): 10-19.

3. Thorvaldsdottir H, Robinson JT, Mesirov JP. Integrative Genomics Viewer (IGV): high-performance genomics data visualization and exploration. Brief Bioinform 2013: 14(2): 178-192.

4. Short KR, Diavatopoulos DA, Reading PC, et al. Using bioluminescent imaging to investigate synergism between Streptococcus pneumoniae and influenza A virus in infant mice. J Vis Exp 2011(50).

5. Schimmel L, Chew KY, Stocks CJ, et al. Endothelial cells are not productively infected by SARS-CoV-2. Clin Transl Immunology 2021: 10(10): e1350.

6. McMillan CLD, Choo JJY, Idris A, et al. Complete protection by a single-dose skin patch-delivered SARS-CoV-2 spike vaccine. Sci Adv 2021; 7: eabj8065.

7. Marshall RJ, Armart P, Hulme KD, et al. Glycemic Variability in Diabetes Increases the Severity of Influenza. mBio 2020; 11: e02841-19.

8. Crowe AR, Yue W. Semi-quantitative Determination of Protein Expression using Immunohistochemistry Staining and Analysis: An Integrated Protocol. Bio Protoc 2019; 9: e3465.

9. Liu X, Quan N. Immune Cell Isolation from Mouse Femur Bone Marrow. Bio Protoc 2015: 5(20).

10. Liao M, Liu Y, Yuan J, et al. Single-cell landscape of bronchoalveolar immune cells in patients with COVID-19. Nat Med 2020: 26(6): 842-844.

11. Hao Y, Hao S, Andersen-Nissen E, et al. Integrated analysis of multimodal single-cell data. Cell 2021: 184(13): 3573-3587 e3529.